International Journal of Solids and Structures 66 (2015) 151–170

Contents lists available at ScienceDirect

International Journal of Solids and Structures

journal homepage: www.elsevier.com/locate/ijsolstr

On large deformation granular strain measures for generating stress–strain relations based upon three-dimensional discrete element simulations

Boning Zhang, Richard A. Regueiro *

Department of Civil, Environmental, and Architectural Engineering, University of Colorado Boulder, Boulder CO 80309, United States

ARTICLE INFO

Article history:
Received 11 August 2014
Received in revised form 17 March 2015
Available online 7 May 2015

Keywords:
Granular materials
Finite strain measures
Discrete Element Method
Large rotation
Cavity expansion
Pile penetration

ABSTRACT

Generating stress–strain relations based upon three-dimensional discrete element simulations, for hierarchical multiscale constitutive modeling of granular materials at finite strain, requires measures of stress and strain in the reference and current configurations. The Cauchy stress tensor calculated from interparticle forces and branch vectors resulting from discrete element simulations, is well-established, but the various finite strain definitions existing in the literature are not as well studied or accepted. Thus, the paper develops seven finite strain measures in three-dimensions (Cartesian coordinates assumed): two are calculated in the reference configuration, and five are calculated in the current configuration. In the process, a time-integrated deformation gradient is formulated, with which the Cauchy stress tensor can be mapped to either the Kirchhoff stress, first Piola–Kirchhoff stress, or second Piola–Kirchhoff stress. The difficulty in calculating strain measures for granular materials is the discrete particulate nature of the materials. In the paper, strain measures are motivated by the equivalent continuum method, but are extended to finite strain in three-dimensions. Simulations are conducted to test the finite strain measures, and it is found that these strain measures are independent of rigid body rotation of a particle assembly. Granular Cauchy stress is also calculated for these discrete element simulations to be able to plot stress–strain curves in the current configuration. Finally, two numerical examples with large deformation are simulated: (1) cavity expansion, and (2) pile penetration; and their results are analyzed.

1. Introduction

Within the context of hierarchical multiscale constitutive modeling for granular materials, it is desirable to calculate stress and strain measures to develop continuum constitutive equations (or to substitute such measures into a continuum computational model such as the Finite Element Method (FEM)), which for generality, should be applicable for large deformations. Examples motivating the need for large deformation analysis of granular materials include cone penetrometer testing to estimate in situ shear strength of sands; pile insertion effects in sand; or cavity expansion in sand due to buried explosives (Regueiro et al., 2013). The calculation of Cauchy stress for granular materials is well-established (Christoffersen et al., 1981; Rothenburg and Selvadurai, 1981; Bagi, 1996), however, for finite strain measures, in particular in three-dimensions (3D), there is to date no conclusive work on the subject. To begin the discussion, we refer to Chang et al. (1992), who broke down granular materials into three different length scales (decreasing in scale) as shown in Fig. 1: (1) representative unit, (2) micro-element, and (3) inter-particle contact. The micro-element scale includes a small assembly composed of one particle surrounded by neighboring particles. The deformation at the micro-element scale and the representative unit scale will be linked together through granular finite strain definitions. The definitions and formulations of micro-mechanical strain will be developed at the micro-element scale (i.e., the tetrahedral cell in a Delaunay tessellation (Bagi, 1996), which links particle centroids as well as provides the averaging volume domain). As just mentioned, there are few existing contributions in the literature that establish a micro-mechanical strain formulation for granular materials suitable for large deformation analysis, let alone in three-dimensions (3D). According to Bagi (2006), Duran et al. (2010) and Fu and Dafalias (2012), these formulations are based upon two possible approaches: (1) the equivalent continuum approach (Bagi, 1996; Kruyt and Rothenburg, 1996; Kuhn, 1999; Cambou et al., 2000; Dedecker et al., 2000; Kruyt, 2003; Tordesillas et al., 2010; Fu and Dafalias, 2012), and (2) the

* Corresponding author.
E-mail address: richard.regueiro@colorado.edu (R.A. Regueiro).

http://dx.doi.org/10.1016/j.ijsolstr.2015.04.012
0020-7683/

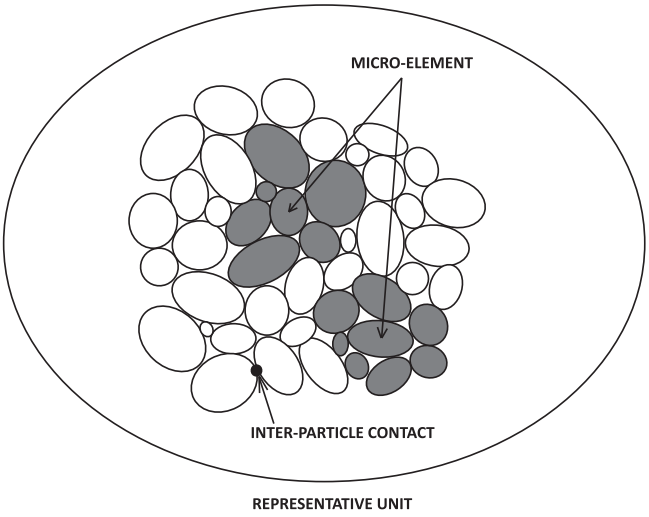

Fig. 1. Schematic representation of three length-scale levels of a granular material, motivated by Chang et al. (1992): (1) inter-particle contact Ω^{contact}, (2) micro-element (which will be a tetrahedron for 3D ellipsoids) Ω^{micro}, (3) sub-domain/RVE/representative-unit $\Omega^{\text{sub-domain}}$, and (4) full assembly Ω^{assembly} (not shown), where $\Omega^{\text{contact}} \subset \Omega^{\text{micro}} \subset \Omega^{\text{sub-domain}} \subseteq \Omega^{\text{assembly}}$.

best-fit approach (Liao et al., 1997; Cambou et al., 2000; Satake, 2004). The difficulty arises when a strain tensor for a granular material is calculated from the Discrete Element Method (DEM), because it is not the same as when calculated for a continuous material using the Finite Element Method (FEM). The classical small strain definition, $\epsilon_{ij} = \frac{1}{2}\left(\frac{\partial u_i}{\partial x_j} + \frac{\partial u_j}{\partial x_i}\right)$, can be used, but it is not easy to calculate a spatial derivative of the particle displacements in a DEM calculation because the particles are discrete (i.e., a continuous displacement field is not immediately identified). As a result, one approach is to replace the granular assembly by a continuous domain (Bagi, 1996). In the equivalent continuous domain the spatial derivatives can be easily calculated , such as by applying the Gauss theorem (Bagi, 1996) or the method used in this paper (i.e., to interpolate particle centroid displacements via linear tetrahedral shape functions, with tetrahedra identified by Delaunay tessellation). Some conditions must be satisfied in order for a domain to be considered an equivalent continuous domain, such as (1) the same kinematics for both the characteristic nodal points and particle centroids (Bagi, 1996, 2006), and (2) convex geometry. This leads to what is known as the *equivalent continuum approach*.

Although there are different micro-mechanical strain measures for granular materials reported in the literature, additional work is still needed on the definition of micro-mechanical strains suitable for large deformation analysis in three-dimensions (3D). Many of the aforementioned strain formulations are based upon the small strain assumption and/or are applied only in two-dimensions (2D), namely they cannot represent large deformations (i.e., large strains *and* rotations) nor are formulated or demonstrated for 3D. Large deformations in granular materials, however, are not unheard of, such as shear banding in sand assemblies, cone penetrometer estimates of in situ shear strength in sand, pile insertion effects in sand, and explosive loading of soils (Alshibli and Alramahi, 2006; Fu and Dafalias, 2012; Chupin et al., 2012; Regueiro et al., 2013). Thus, the small strain assumption is not applicable in these cases, which motivates the development of new granular finite strain measures in 3D.

In the context of finite strain, to our knowledge, there are two potential approaches to calculating strain measures in granular materials based upon DEM simulations. One is using the rate of deformation tensor $\boldsymbol{d}$ proposed by Fu and Dafalias (2012), and although they compared their micro-mechanical strain to macro-wall-strain (i.e., the strain calculated from the boundary displacements), in 2D simulations, they did not show analytically that their measure is valid for large deformations considering also large rigid body rotations of particle assemblies. In addition, they used reference triangles to calculate the micro-element rate of deformation tensor instead of Delaunay tessellation (Bagi, 1996), in order to be able to ensure concave particle assembly shape and avoid noise in the strain calculations (Fu and Dafalias, 2012). Each reference triangle spans a number of particles, and only the velocities of the three vertices are considered. This will lose the contribution and information provided by other particles contained within the reference triangle. This particular definition of rate of deformation tensor by Fu and Dafalias (2012) is closely related to our definition, yet we use a Delaunay tessellation and consider other large deformation granular strain measures (e.g., Lagrangian, Eulerian, and Hencky) and extend to 3D. Another finite strain approach is based upon the accumulation method of Chupin et al. (2012), who used their definition to calculate finite strain in shear bands with Digital Image Correlation (DIC). Although theirs is an experimental study at finite strain, the formulation can be used in a DEM simulation as well. Their formulation, however, is based upon a finite element grid. They did not look into the micro-element level of strain in the soil assembly (Fig. 1).

Another approach to calculating finite strain from discrete element simulation results, was considered in (O'Sullivan et al., 2003), in which they calculated finite strain (the Green–Lagrange strain tensor) from discrete element simulations in two and three dimensions, accounting for particle rotations within the continuum displacement field approximation. In three dimensions, they also espoused the linear tetrahedron to interpolate particle displacements, from which displacement gradients can in turn be easily calculated. To address the non-smooth, or "erratic", displacements of the particles within a shear band where there is localized deformation, for instance, they took advantage of the nonlocality of meshfree interpolation functions (smoothed over a window of defined length scale) to interpolate the particle displacements, and as a result smooth the strain values within a shear band. This is an interesting approach to the problem, however it introduces another aspect to the continuum interpretation of the discrete element results that at the moment we would like to avoid. Such nonlocal, or generalized continuum interpretations of the discrete particle kinematics is worthy of further study, and is of interest to the authors. For now, we address the non-smooth particle displacement behavior by calculating rate quantities of deformation (such as the velocity gradient in the current configuration) and integrating them in time to obtain finite strain measures.

Therefore, because of the lack of appropriate granular finite strain formulations existing in the literature for 3D, the paper develops seven new granular finite strain measures that may be implemented within a DEM code. These granular finite strain measures have been verified, analytically and numerically, that they are independent of rigid body rotation of the particle assembly. On the other hand, the strain of Bagi (1996) cannot pass the large rotation test, even though Bagi (2006) and Duran et al. (2010) stated that the strain measure of Bagi (1996) is the most accurate formulation when comparing granular strain with the macro-wall-strain (i.e., the strain calculated based upon the boundary displacements). The comparison to macro-wall-strain alone is not a sufficient test of a granular finite strain measure, and thus we introduce a large rotation test, as well as consider two numerical examples demonstrating large deformations in granular materials (cavity expansion and pile penetration).

Among these aforementioned strain measures, there are two micro-polar strains that consider particle rotation as well as particle

translation (Kruyt, 2003; Tordesillas et al., 2010). Bonelli et al. (2012) have shown that particle rotations need only be considered for sub-domains with few particles. Since sub-domains with few particles (they comprise the micro-element scale instead of the representative unit scale in the sense of Chang et al. (1992) in Fig. 1) cannot represent a classical continuum granular strain, we ensure that the granular strain calculations are based upon representative unit scale (i.e., the sub-domain scale) DEM calculations. Considering particle rotations in micropolar strain measures requires further study beyond the scope of the paper, and is of interest to the authors. Thus, (1) the granular finite strain measures proposed in the paper will also neglect particle rotations, and (2) formulations are based upon the *equivalent continuum approach* and Delaunay tessellation (similar to Bagi (1996)), but are extended for finite strain and 3D. In addition, with the Representative Volume Element (RVE) (also known as, the representative unit or sub-domain), the strain and stress spatial distribution for any full assembly can be obtained in 3D. In Fu and Dafalias (2012), they showed that with smaller reference triangles, higher spatial resolution can be obtained. Thus, the Delaunay tessellation that is used to calculate strain in Bagi (1996) is a good choice. However, (3) formulations here will take advantage of the interpolation method of isoparametric finite elements instead of applying the divergence theorem, where Bagi (1996), Kruyt and Rothenburg (1996) and Kuhn (1999) used the divergence theorem. We note that Fu and Dafalias (2012) also used the interpolation method to achieve their finite strain measure. However, in this paper we also calculate granular Lagrangian and Eulerian strains in 3D, instead of just the rate of deformation tensor in 2D (Fu and Dafalias, 2012). In addition, attention is paid to two different volume averaging methods during the derivation of granular Lagrangian and Eulerian strain measures (these two averaging methods are: *individual average definition* and *total quadratic term definition* as in Section 3.1.2). The paper proves analytically that the finite strain formulations are independent of rigid body rotation of particle assemblies/sub-domains. Comparisons with macro-wall-strains are also achieved.

Granular finite strain measures proposed in the paper can be applied not only to DEM simulation results, but also for the post-processing of experimental data to calculate finite granular strains for assemblies of particles. This can be achieved with an appropriate particle tracking method (Ando et al., 2012; Druckrey and Alshibli, 2014). The procedures to calculate granular strain in experiments are similar to Alshibli and Alramahi (2006). The formulation in Alshibli and Alramahi (2006), however, is not suitable for comparison to the results in this paper, because Alshibli and Alramahi (2006) did not obtain their strain values for representative units (sub-domains/RVEs), but only for groups of $\approx$10 particles (i.e., the micro-element scale).

The formulation of the Cauchy stress tensor has been well established and agreed upon by various publications in the literature, such as Christoffersen et al. (1981), Rothenburg and Selvadurai (1981) and Bagi (1996), and thus is not re-derived in the paper.

With regard to notation, lower case symbols are used to represent variables, or indices of a tensor, in the current configuration, while upper case symbols are used to represent variables, or indices of a tensor, in the reference configuration. For example, $\boldsymbol{X}^{\alpha}$ is the position vector of centroid of particle α in the reference configuration $\mathcal{B}_0$, and $\boldsymbol{x}^{\alpha}$ is its position vector in the current configuration $\mathcal{B}_t$(parameterized with time t). Einstein's convention of summation over repeated indices is implied (Eringen, 1962).

An outline of the remainder of the paper is as follows: Section 2 discusses how a continuous domain is generated connecting particle centroids via a Delaunay tessellation; Section 3 reviews the Bagi strain tensor, derives new granular finite strain measures, and tests them by (i) comparison to macro-wall-strain calculations, and (ii) via a large rotation test of a particle assembly; Section 4 presents two numerical examples demonstrating large deformation (cavity expansion, and pile penetration); and Section 5 provides conclusions.

2. Replacement of granular assembly by continuous domain

The formulation of Bagi (1996) for granular stress is based upon the Voronoi cell approximation representing contacting grains, while the strain calculations are based upon the Delaunay tessellation of the granular assemblies as shown in Fig. 2. The Delaunay tessellation can be generated by Barber et al. (1996), which is used as the equivalent continuous domain for Bagi's formulation of small strain tensor as well as the method proposed in this paper. Briefly speaking, this tessellation will split the granular assembly into many tetrahedrons whose vertices are the particle centroids. Each edge of a tetrahedron will connect the centroids of two particles, where these two particles are not necessarily in contact with each other. If they are in contact, then the edge will represent a *real* contact or simply a *contact* (Bagi, 1996). If they are not in contact, then the edge will represent a *virtual* contact (Bagi, 1996).

With the tessellation, a full granular assembly is easily represented by a series of continuous sub-domains/RVEs, in which the nodes of the tetrahedrons will have the same kinematics—such as displacement, velocity, and acceleration—as the granular material particle centroids. The kinematic state of these points in the equivalent continuous domain will remain the same as in the granular assembly simulated by DEM; thus, the results for granular strain are consistent between the continuous (tessellated) and discrete (DEM) representations of a granular material.

3. Granular finite strain tensors

In this section, eight different formulations of granular strain tensor will be presented: one small strain tensor is proposed by Bagi (1996), and seven new finite strain measures are derived.

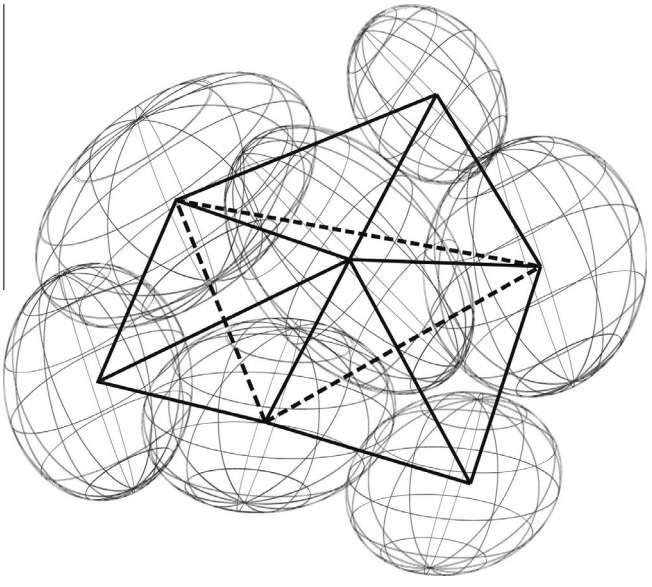

Fig. 2. Delaunay tessellation of seven ellipsoidal particles showing four tetrahedrons, which is the *micro-element length scale* according to Chang et al. (1992). The dashed lines indicate the hidden lines that connect the centroids of those ellipsoidal particles toward the back of the assembly, and the solid lines are the visible lines connecting the centroids of those particles toward the front.

The motivation to derive the seven new finite strain formulations is to be able to represent finite strains accurately (including large rotations of particle assemblies), since Bagi's granular strain is based upon the small strain assumption. We may encounter many cases for which the small strain assumption is not valid, such as sand grains under explosive loading, or large shearing during tire rolling or pile penetration.

It is noted that the finite strain measures developed in this paper are suitable for calculating finite strain from spatial gradients of particle displacements provided either by a DEM simulation or an X-ray computed tomography experiment over a volume averaging domain defined by the modeler, whereas Bagi's definition of strain is suitable only at a micro-element level (see Fig. 1) and only for small strains.

After the definitions of these granular strain tensors are presented, two tests are conducted in 3D to check the validity of the measures: (1) comparison of granular strain tensor normal components with macro-wall-strain calculations, and (2) a large rotation test.

3.1. Definitions of granular strain

The granular strain of Bagi (1996) is based upon the Gauss theorem, while the calculation of (1) granular Lagrangian strain, (2) granular Eulerian strain, (3) granular Hencky strain, (4) granular Eulerian strain by rate-form, (5) granular Lagrangian strain by rate-form deformation gradient, (6) granular Eulerian strain by rate-form deformation gradient, and (7) granular Hencky strain by rate-form deformation gradient, take advantage of the interpolation quality of isoparametric finite elements in the Finite Element Method (FEM). But all of them are based upon a Delaunay tessellation (Bagi, 1996). Here, the formulation of Bagi's strain will be briefly summarized, and more attention will be paid to the derivation of the granular Lagrangian, Eulerian, and Hencky strains.

3.1.1. Bagi's granular strain

In Bagi (1996), the average displacement gradient tensor $\overline{\nabla \boldsymbol{u}}$ is derived based upon the divergence theorem and geometric relations. Then, the symmetric part of the average displacement gradient tensor will become the average granular small strain tensor $\overline{\boldsymbol{\epsilon}}$. The formulation of Bagi's granular displacement gradient tensor is as follows,

$$\overline{u_{i,j}} = \frac{1}{V}\sum_{p<q} \Delta u_i^{pq} d_j^{pq}, \quad \Delta u_i^{pq} = u_i^p - u_i^q \tag{1}$$

where the sub-domain volume V, over which the average value is calculated, is based upon the Delaunay tessellation, and $p$and $q$are two nodes of a connecting edge (Fig. 3). Here, $p < q$ is used to make sure that each edge is only calculated once. $\boldsymbol{d}^{pq}$ is the complementary area vector of edge pair (p, q), and can be calculated as,

$$d_i^{pq} = \frac{1}{12}\sum_{tet=1}^{n_{tet}} \left(b_i^{q(tet)} - b_i^{p(tet)}\right) \tag{2}$$

where the vector is summed over the number of tetrahedra n_{tet} in the sub-domain that contains the edge (p, q), which requires our code to know every edge that a cell contains, and $\boldsymbol{b}^{p(tet)}$ is the out-ward area-vector of face $p$which is opposite to node $p$in tetrahedron *tet*. The formulation of $\boldsymbol{d}^{pq}$ can be more easily understood by viewing Fig. 3. $\boldsymbol{u}^p$ is the displacement of node p, which is coincident with the centroidal displacement of particle p. Note that for a classical continuum definition of strain, the individual rotations of particles are not used. Such strain definitions can be extended for generalized continua, such as for micro-polar continua (Kruyt, 2003).

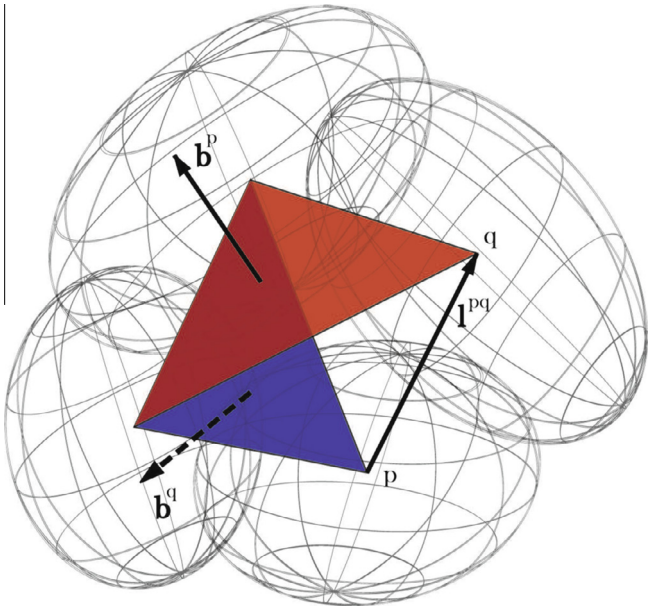

Fig. 3. Illustration of the calculation of the complementary area vector $\boldsymbol{d}^{pq}$, motivated by Duran et al. (2010).

Remark. As the sub-domain deforms (i.e., particles translate and rotate), the initial tessellation will soon not be valid (i.e., a tetrahedron may become highly distorted such that it could invert on itself, making the calculation of displacement gradient invalid), thus the tessellation needs to be updated. A threshold strain value can be used to control the frequency of tessellation update, namely when a component of the incremental strain $\delta\epsilon_{ij}$ reaches the threshold value, then the tessellation will be updated, where $\delta\epsilon_{ij}$ is calculated based upon the strain value at the beginning of the current tessellation as $\delta\epsilon_{ij} = \epsilon_{ij} - \epsilon_{ij(0)}$, where ϵ_{ij} is the current granular strain, and $\epsilon_{ij(0)}$ is the granular strain at the beginning of the current tessellation. Here, the absolute value of each individual component of $\delta\epsilon_{ij}$ will be checked to determine if the tessellation needs to be updated.

3.1.2. Granular Lagrangian strain

The granular Lagrangian strain tensor is formulated as if for a continuous material with displacement fields interpolated by FE shape functions. The spatial derivative of the current particle centroid displacement $\boldsymbol{u}$ with respect to reference position $\boldsymbol{X}$ is then calculated in this equivalent continuous domain. Since Barber et al. (1996) currently just provides 4-noded tetrahedral cells based upon Delaunay tessellation, linear tetrahedral shape functions are used to interpolate the particle displacements. A summary is only provided here, with some details provided in Appendix A, and further details in Felippa (2011). Assuming the four nodes of the tetrahedron are labeled a, b, c, d, the particle a/nodal displacements are $\boldsymbol{u}^a = (u_1^a, u_2^a, u_3^a)$, and we may write the displacement gradient as,

$$\frac{\partial \boldsymbol{u}}{\partial \boldsymbol{X}} = \frac{1}{6V^{tet}} \begin{bmatrix} u_1^a & u_1^b & u_1^c & u_1^d \\ u_2^a & u_2^b & u_2^c & u_2^d \\ u_3^a & u_3^b & u_3^c & u_3^d \end{bmatrix} \begin{bmatrix} \omega_a & \theta_a & \pi_a \\ \omega_b & \theta_b & \pi_b \\ \omega_c & \theta_c & \pi_c \\ \omega_d & \theta_d & \pi_d \end{bmatrix} \tag{3}$$

where V^{tet} is the reference volume of the tetrahedron, and the ω, θ, π parameters are related to the global nodal coordinates, with further details provided in Appendix A.

Since the displacement gradient tensor $\frac{\partial \boldsymbol{u}}{\partial \boldsymbol{X}}$ is constant in each *tet*, the volume integrals can be calculated in a straightforward manner as,

$$\begin{aligned}
&\int_{V^{tet}} \left(\frac{\partial \boldsymbol{u}}{\partial \boldsymbol{X}}\right) dV = V^{tet}\left(\frac{\partial \boldsymbol{u}}{\partial \boldsymbol{X}}\right)\\
&\int_{V^{tet}} \left(\frac{\partial \boldsymbol{u}}{\partial \boldsymbol{X}}\right)^T dV = V^{tet}\left(\frac{\partial \boldsymbol{u}}{\partial \boldsymbol{X}}\right)^T\\
&\int_{V^{tet}} \left(\frac{\partial \boldsymbol{u}}{\partial \boldsymbol{X}}\right)^T \left(\frac{\partial \boldsymbol{u}}{\partial \boldsymbol{X}}\right) dV = V^{tet}\left(\frac{\partial \boldsymbol{u}}{\partial \boldsymbol{X}}\right)^T \left(\frac{\partial \boldsymbol{u}}{\partial \boldsymbol{X}}\right)
\end{aligned} \tag{4}$$

Granular finite strain: Recall the Lagrangian strain tensor from continuum mechanics (Holzapfel, 2000): $\boldsymbol{E} = \left(\boldsymbol{F}^T\boldsymbol{F} - \boldsymbol{I}\right)/2$. With the displacement gradient tensor $\frac{\partial \boldsymbol{u}}{\partial \boldsymbol{X}}$, the granular Lagrangian strain tensor over the sub-domain is derived as,

$$\begin{aligned}
\overline{\boldsymbol{E}} &= \frac{1}{V}\sum_{tet}\left(V^{tet}\overline{\boldsymbol{E}}^{tet}\right) = \frac{1}{V}\sum_{tet}\left[V^{tet}\frac{1}{V^{tet}}\int_{V^{tet}}\frac{1}{2}\left(\boldsymbol{F}^T\boldsymbol{F} - \boldsymbol{I}\right)dV\right]\\
&= \frac{1}{2V}\sum_{tet}\int_{V^{tet}}\left[\left(\frac{\partial \boldsymbol{u}}{\partial \boldsymbol{X}}\right) + \left(\frac{\partial \boldsymbol{u}}{\partial \boldsymbol{X}}\right)^T + \left(\frac{\partial \boldsymbol{u}}{\partial \boldsymbol{X}}\right)^T\left(\frac{\partial \boldsymbol{u}}{\partial \boldsymbol{X}}\right)\right]dV
\end{aligned} \tag{5}$$

With this definition, we calculate $\left(\frac{\partial \boldsymbol{u}}{\partial \boldsymbol{X}}\right)^T\left(\frac{\partial \boldsymbol{u}}{\partial \boldsymbol{X}}\right)$ directly for each tetrahedron, and then obtain its volume average as a whole. Then, this term is called a *total quadratic term definition*. On the other hand, another possible definition is the following,

$$\overline{\boldsymbol{E}} = \frac{1}{2}\left[\left(\frac{\partial \overline{\boldsymbol{u}}}{\partial \boldsymbol{X}}\right) + \left(\frac{\partial \overline{\boldsymbol{u}}}{\partial \boldsymbol{X}}\right)^T + \left(\frac{\partial \overline{\boldsymbol{u}}}{\partial \boldsymbol{X}}\right)^T\left(\frac{\partial \overline{\boldsymbol{u}}}{\partial \boldsymbol{X}}\right)\right] \tag{6}$$

which can be called an *individual average definition*, since the individual average displacement gradient tensor $\left(\frac{\partial \overline{\boldsymbol{u}}}{\partial \boldsymbol{X}}\right)$ has been used, where

$$\frac{\partial \overline{\boldsymbol{u}}}{\partial \boldsymbol{X}} \overset{\text{def}}{=} \frac{1}{V}\sum_{tet}\int_{V^{tet}}\frac{\partial \boldsymbol{u}}{\partial \boldsymbol{X}}dV = \frac{1}{V}\sum_{tet}\left(V^{tet}\frac{\partial \boldsymbol{u}}{\partial \boldsymbol{X}}\right) \tag{7}$$

The difference between these two definitions will be discussed further in Section 3.2.

3.1.3. Granular Eulerian strain

To calculate the granular Eulerian strain, the equivalent continuous domain and interpolation functions are similarly used as for the Lagrangian strain definition, except that the spatial derivative is taken with respect to the current particle coordinates, instead of the reference particle coordinates. Note that the direct formulation for granular Eulerian strain would be written as,

$$\overline{\boldsymbol{e}} = \frac{1}{2v}\sum_{tet}\int_{v^{tet}}\left[-\left(\frac{\partial \boldsymbol{u}}{\partial \boldsymbol{x}}\right)^{-1} - \left(\frac{\partial \boldsymbol{u}}{\partial \boldsymbol{x}}\right)^{-T} - \left(\frac{\partial \boldsymbol{u}}{\partial \boldsymbol{x}}\right)^{-T}\left(\frac{\partial \boldsymbol{u}}{\partial \boldsymbol{x}}\right)^{-1}\right]dv \tag{8}$$

where v is the total deformed sub-domain volume. This direct formulation, however, cannot be used in a computer code because the granular Eulerian strain requires the calculation $\left(\frac{\partial \boldsymbol{u}}{\partial \boldsymbol{x}}\right)^{-1}$, which may be singular when the displacement gradient is very small at the beginning of simulation. Thus, an equivalent Eulerian formulation without the inverse operation is needed. Referring to Holzapfel (2000), we may derive the continuum Eulerian strain as,

$$\boldsymbol{e} = \frac{1}{2}\left[\frac{\partial \boldsymbol{u}}{\partial \boldsymbol{x}} + \left(\frac{\partial \boldsymbol{u}}{\partial \boldsymbol{x}}\right)^T - \left(\frac{\partial \boldsymbol{u}}{\partial \boldsymbol{x}}\right)^T\left(\frac{\partial \boldsymbol{u}}{\partial \boldsymbol{x}}\right)\right] \tag{9}$$

Thus, the average granular Eulerian strain with *total quadratic term definition* is,

$$\overline{\boldsymbol{e}} = \frac{1}{2v}\sum_{tet}v^{tet}\left[\frac{\partial \boldsymbol{u}}{\partial \boldsymbol{x}} + \left(\frac{\partial \boldsymbol{u}}{\partial \boldsymbol{x}}\right)^T - \left(\frac{\partial \boldsymbol{u}}{\partial \boldsymbol{x}}\right)^T\left(\frac{\partial \boldsymbol{u}}{\partial \boldsymbol{x}}\right)\right] \tag{10}$$

and the granular Eulerian strain tensor with *individual average definition* is,

$$\overline{\boldsymbol{e}} = \frac{1}{2}\left[\left(\frac{\partial \overline{\boldsymbol{u}}}{\partial \boldsymbol{x}}\right) + \left(\frac{\partial \overline{\boldsymbol{u}}}{\partial \boldsymbol{x}}\right)^T - \left(\frac{\partial \overline{\boldsymbol{u}}}{\partial \boldsymbol{x}}\right)^T\left(\frac{\partial \overline{\boldsymbol{u}}}{\partial \boldsymbol{x}}\right)\right] \tag{11}$$

where

$$\frac{\partial \overline{\boldsymbol{u}}}{\partial \boldsymbol{x}} \overset{\text{def}}{=} \frac{1}{v}\sum_{tet}\int_{v^{tet}}\frac{\partial \boldsymbol{u}}{\partial \boldsymbol{x}}dv = \frac{1}{v}\sum_{tet}\left(v^{tet}\frac{\partial \boldsymbol{u}}{\partial \boldsymbol{x}}\right) \tag{12}$$

In the granular Eulerian strain calculation, the current volume of each tetrahedron v^{tet}, and total current volume of the continuously-tessellated averaging sub-domain v will be used.

3.1.4. Granular Hencky strain

In addition, the granular Hencky strain can be calculated based upon the average deformation gradient tensor $\overline{\boldsymbol{F}}$. The average deformation gradient tensor can be calculated from the average Eulerian displacement gradient tensor in Eq. (12) as

$$\overline{\boldsymbol{F}} = \left(\boldsymbol{1} - \frac{\partial \overline{\boldsymbol{u}}}{\partial \boldsymbol{x}}\right)^{-1} \tag{13}$$

Then the granular Hencky strain $\overline{\boldsymbol{e}}^H$ can be calculated as

$$\overline{\boldsymbol{e}}^H = ln\sqrt{\overline{\boldsymbol{b}}}, \quad \overline{\boldsymbol{b}} = \overline{\boldsymbol{F}}\,\overline{\boldsymbol{F}}^T \tag{14}$$

where $ln(\bullet)$ and $\sqrt{(\bullet)}$ are matrix operations (natural logarithm, and square root, respectively).

3.1.5. Granular Eulerian strain based upon the rate of deformation tensor

Besides the above two finite strain formulations for granular materials for the *individual average definition* (which we will choose based upon the results in Section 3.2), Eqs. (6) and (11), the Eulerian strain can also be calculated from the time integration of its Lie derivative. The advantage to this formulation is to recognize that in a DEM simulation, particles may experience large relative displacements, such that the particles cross paths (or inter-mix) over a certain number of time steps (i.e., these are material point motions that are disallowed in continuum mechanics, which states that such motions must be smooth, for which the Jacobian of deformation $J = det\boldsymbol{F} > 0$ (Truesdell and Toupin, 1960)). Because the dynamic balance of linear momentum and angular momentum equations of DEM are usually integrated in time explicitly (e.g., central difference in time), small time steps are used, thus an incremental calculation of strain in the current configuration is warranted. First, the deformation rate tensor for a granular material is introduced.

(1) Deformation rate for granular materials. Recall the definition of the deformation rate tensor $\overline{\boldsymbol{d}}$ as the symmetric part of the velocity gradient $\frac{\partial \overline{\boldsymbol{v}}}{\partial \boldsymbol{x}}$ (both written as averages for the granular strain definition), such that,

$$\overline{\boldsymbol{d}} = \frac{1}{2}\left[\frac{\partial \overline{\boldsymbol{v}}}{\partial \boldsymbol{x}} + \left(\frac{\partial \overline{\boldsymbol{v}}}{\partial \boldsymbol{x}}\right)^T\right] \tag{15}$$

where

$$\frac{\partial \boldsymbol{v}}{\partial \boldsymbol{x}} = \frac{1}{6v^{tet}}\begin{bmatrix} v_1^a & v_1^b & v_1^c & v_1^d\\ v_2^a & v_2^b & v_2^c & v_2^d\\ v_3^a & v_3^b & v_3^c & v_3^d\end{bmatrix}\begin{bmatrix}\omega_a & \theta_a & \pi_a\\ \omega_b & \theta_b & \pi_b\\ \omega_c & \theta_c & \pi_c\\ \omega_d & \theta_d & \pi_d\end{bmatrix}, \quad \frac{\partial \overline{\boldsymbol{v}}}{\partial \boldsymbol{x}} \overset{\text{def}}{=} \frac{1}{v}\sum_{tet=1}^{n_{tet}}\left(v^{tet}\frac{\partial \boldsymbol{v}}{\partial \boldsymbol{x}}\right) \tag{16}$$

Thus, the granular spatial velocity gradient $\bar{\boldsymbol{l}}$ and deformation rate $\bar{\boldsymbol{d}}$ tensors will be,

$$\bar{\boldsymbol{l}} = \frac{\overline{\partial \boldsymbol{v}}}{\partial \boldsymbol{x}}, \quad \bar{\boldsymbol{d}} = sym(\bar{\boldsymbol{l}}) \tag{17}$$

(2) Granular Eulerian strain by rate form. It is possible to show (Holzapfel, 2000) that the Lie derivative of the Eulerian strain $\mathcal{L}_{\boldsymbol{v}}\boldsymbol{e}$, with respect to the current velocity $\boldsymbol{v}$, is equal to the rate of deformation tensor $\boldsymbol{d}$ as,

$$\mathcal{L}_{\boldsymbol{v}}\boldsymbol{e} \overset{\text{def}}{=} \dot{\boldsymbol{e}} + \boldsymbol{l}^T\boldsymbol{e} + \boldsymbol{e}\boldsymbol{l} = \boldsymbol{d} \tag{18}$$

By definition, the Lie derivative is objective (Holzapfel, 2000) with respect to arbitrary rigid body motions of the granular assembly in the current configuration. We then apply a semi-implicit time integration scheme to obtain the granular Eulerian strain by rate-form at current time t_{n+1} as,

$$\boldsymbol{e}_{n+1} = \boldsymbol{e}_n + \left(\boldsymbol{d}_{n+1} - \boldsymbol{l}^T_{n+1}\boldsymbol{e}_n - \boldsymbol{e}_n\boldsymbol{l}_{n+1}\right)\Delta t \tag{19}$$

where $\Delta t = t_{n+1} - t_n$ is the time increment over which strain is calculated (i.e., it is *not* the actual time increment used in the central difference in time integration). Based on Eq. (19), the *granular Eulerian strain by rate-form* using Eq. (17) can be calculated as,

$$\bar{\boldsymbol{e}}_{n+1} = \bar{\boldsymbol{e}}_n + \left(\bar{\boldsymbol{d}}_{n+1} - \bar{\boldsymbol{l}}^T_{n+1}\bar{\boldsymbol{e}}_n - \bar{\boldsymbol{e}}_n\bar{\boldsymbol{l}}_{n+1}\right)\Delta t \tag{20}$$

3.1.6. Granular deformation gradient based upon the velocity gradient, and associated finite strain measures

Similar to how the *granular Eulerian strain by rate-form* is calculated in Section 3.1.5 by a semi-implicit time integration of the Lie derivative of the Eulerian strain over a *calculation time interval* Δt (i.e., *not* the time step of the central difference in time integration of the DEM balance of linear and angular momentum equations), here we integrate in time the velocity gradient to calculate a *granular deformation gradient by rate-form* and associated granular finite strain definitions. We start with the classical definition of the velocity gradient in the current configuration as,

$$\boldsymbol{l} = \dot{\boldsymbol{F}}\boldsymbol{F}^{-1} \tag{21}$$

where the time derivative of $\boldsymbol{F}$ may then be written as,

$$\dot{\boldsymbol{F}} = \boldsymbol{l}\boldsymbol{F} \tag{22}$$

We integrate Eq. (22) over the *calculation time interval* Δt such that a Backward Euler time integration for the deformation gradient at current time t_{n+1} is written as,

$$\bar{\boldsymbol{F}}_{n+1} = \left(\boldsymbol{1} - \Delta t\,\bar{\boldsymbol{l}}_{n+1}\right)^{-1}\bar{\boldsymbol{F}}_n \tag{23}$$

and a semi-implicit time integration leads to,

$$\bar{\boldsymbol{F}}_{n+1} = \left(\boldsymbol{1} + \Delta t\,\bar{\boldsymbol{l}}_{n+1}\right)\bar{\boldsymbol{F}}_n \tag{24}$$

We can now write *directly* the granular finite strain measures, such as the *granular Lagrangian strain by rate-form deformation gradient*,

$$\bar{\boldsymbol{E}}_{n+1} = \frac{1}{2}\left(\bar{\boldsymbol{F}}^T_{n+1}\bar{\boldsymbol{F}}_{n+1} - \boldsymbol{1}\right) \tag{25}$$

and the *granular Eulerian strain by rate-form deformation gradient*,

$$\bar{\boldsymbol{e}}_{n+1} = \frac{1}{2}\left(\boldsymbol{1} - \bar{\boldsymbol{b}}^{-1}_{n+1}\right), \quad \bar{\boldsymbol{b}}_{n+1} = \bar{\boldsymbol{F}}_{n+1}\bar{\boldsymbol{F}}^T_{n+1} \tag{26}$$

and the *granular Hencky strain by rate-form deformation gradient*,

$$\bar{\boldsymbol{e}}^H_{n+1} = ln\sqrt{\bar{\boldsymbol{b}}_{n+1}} \tag{27}$$

From a finite strain constitutive modeling perspective, the *granular velocity gradient* $\bar{\boldsymbol{l}}_{n+1}$ and the *granular deformation gradient by rate-form* $\bar{\boldsymbol{F}}_{n+1}$ are the fundamental deformation measures to drive a constitutive model subroutine (i.e., rate-based, or direct integration). Also, the granular finite strains in Eqs. (25)–(27) provide sufficient measures to which to compare to experimental data in terms of constitutive model development. The *granular Eulerian strain by rate-form* and *granular Eulerian strain by rate-form deformation gradient* yield the same values, thus we only show results once for both strain measures, and then going forward only use the *granular Eulerian strain by rate-form deformation gradient*.

3.2. Tests of granular strains

For *direct* calculations of granular Lagrangian and Eulerian strains in Eqs. (6) and (11) (i.e., not the *rate-form* expressions nor the Hencky strain), two different sets of formulations can be obtained based upon the *total quadratic term definition* and the *individual average definition*. Formulations based upon the two different definitions will be identical for the small strain case. They show, however, significant differences in the finite strain case, which comes from the different averaging approaches for the quadratic term. Consider an assembly containing only two *tets*, *a* and *b*, as an example to explain the difference, see Fig. 4.

The normal component of the quadratic term in the x_1 direction when calculated with the *total quadratic term definition* is as follows,

$$\frac{1}{v}\sum_{tet}\left[v^{tet}\left(\frac{\partial u_1}{\partial x_1}\right)^{tet}\left(\frac{\partial u_1}{\partial x_1}\right)^{tet}\right] = \frac{1}{v}\left[v^a\left(\frac{\partial u_1}{\partial x_1}\right)^a\left(\frac{\partial u_1}{\partial x_1}\right)^a + v^b\left(\frac{\partial u_1}{\partial x_1}\right)^b\left(\frac{\partial u_1}{\partial x_1}\right)^b\right] \tag{28}$$

The normal component of the quadratic term in the x_1 direction when calculated with the *individual average definition* is as follows,

$$\begin{aligned}
&\left(\frac{1}{v}\sum_{tet}\left[v^{tet}\left(\frac{\partial u_1}{\partial x_1}\right)^{tet}\right]\right)\left(\frac{1}{v}\sum_{tet}\left[v^{tet}\left(\frac{\partial u_1}{\partial x_1}\right)^{tet}\right]\right)\\
&= \frac{1}{v}\left[v^a\left(\frac{\partial u_1}{\partial x_1}\right)^a + v^b\left(\frac{\partial u_1}{\partial x_1}\right)^b\right]\frac{1}{v}\left[v^a\left(\frac{\partial u_1}{\partial x_1}\right)^a + v^b\left(\frac{\partial u_1}{\partial x_1}\right)^b\right]\\
&= \frac{1}{v^2}\left[(v^a)^2\left(\frac{\partial u_1}{\partial x_1}\right)^a\left(\frac{\partial u_1}{\partial x_1}\right)^a + (v^b)^2\left(\frac{\partial u_1}{\partial x_1}\right)^b\left(\frac{\partial u_1}{\partial x_1}\right)^b\right]\\
&\quad + 2\left(\frac{v^a}{v}\right)\left(\frac{v^b}{v}\right)\left(\frac{\partial u_1}{\partial x_1}\right)^a\left(\frac{\partial u_1}{\partial x_1}\right)^b
\end{aligned} \tag{29}$$

where v is the total volume of the averaging sub-domain, and v^a and v^b are the volumes of each *tet* in Fig. 4. In the *total quadratic term definition*, the quadratic term will be a linear function of $\frac{v^{tet}}{v}$, while in the *individual average definition*, the term will be a quadratic function of $\frac{v^{tet}}{v}$. Since $\frac{v^{tet}}{v} \leqslant 1$ always holds, the quadratic term in the *total quadratic term definition* will be larger than or equal to that in the *individual average definition*. As the assembly becomes larger with more particles, $\frac{v^{tet}}{v}$ will become smaller, and then the quadratic term in the *total quadratic term definition* will become noticeably larger than that in the *individual average definition*.

With this difference, granular finite strain calculated from the two definitions will be noticeably different for large deformation. Results show that finite strain calculated from the *total quadratic term definition* is large compared to the wall strain value. Fig. 5 shows the granular strains based upon the *total quadratic term definition* as compared to the *individual average definition* and wall strain for the isotropic compression of an assembly with 52 F-75 Quartz Ottawa sand grains. The Lagrangian strain and Eulerian strain based upon the *total quadratic term definition* are much larger than the corresponding *individual average definition*, which are comparable to the macro-wall-strain. This means that the quadratic terms in the strain formulations based upon the *total quadratic term definition* are larger, and lead to erroneous results when compared to the macro-wall-strain. Also, we show in the

numerical examples later (for cavity expansion and pile penetration) that the time-integrated deformation gradient $\overline{\boldsymbol{F}}_{n+1}$ and associated strain measures are the proper measures to use given the tendency for grains to inter-mix during large deformations such as encountered during cavity expansion or pile penetration. This in turn supports the *individual average definition* interpretation, because when calculating the Lagrangian strain from the deformation gradient, the displacement gradient terms are multiplied together individually, rather than averaging the quadratic term directly. This is why we prefer the *individual average definition*.

The difference between the wall strain volumetric strain value and the linear Bagi and finite Lagrangian and Eulerian volumetric strain values (based upon the *individual average definition*) in Fig. 5 is due to the difference in the volumes used to calculate the average strain values. For the wall strain, the volume is the cross-section multiplied by the current length of the box which initially is 1.78 mm^3, and for the other strain values the Delaunay tessellation is used to calculate the total averaging volume, which initially is 1.26 mm^3, 70.8% of the wall volume. The linear Bagi and finite Lagrangian and Eulerian strain values are different based upon their different definitions.

The aforementioned formulations of Bagi's strain, granular Lagrangian and Eulerian strains based upon the *individual average definition*, granular Hencky strain, granular Eulerian strain by rate-form, granular Lagrangian strain by rate-form deformation gradient, granular Eulerian strain by rate-form deformation gradient, and granular Hencky strain by rate-form deformation gradient, are summarized as follows,

1. Bagi's small strain: $\overline{\boldsymbol{\epsilon}}^{Bagi} = \frac{1}{2}\left[\overline{\nabla(\boldsymbol{u})} + \overline{\nabla(\boldsymbol{u})}^T\right]$
2. linear Lagrangian strain: $\overline{\boldsymbol{E}}^{lin} = \frac{1}{2}\left[\left(\frac{\overline{\partial \boldsymbol{u}}}{\partial \boldsymbol{X}}\right) + \left(\frac{\overline{\partial \boldsymbol{u}}}{\partial \boldsymbol{X}}\right)^T\right]$
3. linear Eulerian strain: $\overline{\boldsymbol{e}}^{lin} = \frac{1}{2}\left[\left(\frac{\overline{\partial \boldsymbol{u}}}{\partial \boldsymbol{x}}\right) + \left(\frac{\overline{\partial \boldsymbol{u}}}{\partial \boldsymbol{x}}\right)^T\right]$
4. Bagi finite strain: $\overline{\boldsymbol{\epsilon}}^{Bagi,finite} = \frac{1}{2}\left[\overline{\nabla(\boldsymbol{u})} + \overline{\nabla(\boldsymbol{u})}^T - \overline{\nabla(\boldsymbol{u})}^T\overline{\nabla(\boldsymbol{u})}\right]$, where the average displacement gradient tensor is calculated by Eq. (1).
5. Lagrangian strain: $\overline{\boldsymbol{E}} = \frac{1}{2}\left[\left(\frac{\overline{\partial \boldsymbol{u}}}{\partial \boldsymbol{X}}\right) + \left(\frac{\overline{\partial \boldsymbol{u}}}{\partial \boldsymbol{X}}\right)^T + \left(\frac{\overline{\partial \boldsymbol{u}}}{\partial \boldsymbol{X}}\right)^T\left(\frac{\overline{\partial \boldsymbol{u}}}{\partial \boldsymbol{X}}\right)\right]$
6. Eulerian strain: $\overline{\boldsymbol{e}} = \frac{1}{2}\left[\left(\frac{\overline{\partial \boldsymbol{u}}}{\partial \boldsymbol{x}}\right) + \left(\frac{\overline{\partial \boldsymbol{u}}}{\partial \boldsymbol{x}}\right)^T - \left(\frac{\overline{\partial \boldsymbol{u}}}{\partial \boldsymbol{x}}\right)^T\left(\frac{\overline{\partial \boldsymbol{u}}}{\partial \boldsymbol{x}}\right)\right]$
7. Hencky strain: $\overline{\boldsymbol{e}}^H = ln\sqrt{\overline{\boldsymbol{b}}}$, $\overline{\boldsymbol{b}} = \overline{\boldsymbol{F}}\,\overline{\boldsymbol{F}}^T$
8. Eulerian strain by rate-form: $\overline{\boldsymbol{e}}^{rate}_{n+1} = \overline{\boldsymbol{e}}_n + \left(\overline{\boldsymbol{d}}_{n+1} - \overline{\boldsymbol{l}}^T_{n+1}\overline{\boldsymbol{e}}_n - \overline{\boldsymbol{e}}_n\overline{\boldsymbol{l}}_{n+1}\right)\Delta t$
9. Lagrangian strain by rate-form deformation gradient: $\overline{\boldsymbol{E}}_{n+1} = \frac{1}{2}\left(\overline{\boldsymbol{F}}^T_{n+1}\overline{\boldsymbol{F}}_{n+1} - \boldsymbol{1}\right)$
10. Eulerian strain by rate-form deformation gradient: $\overline{\boldsymbol{e}}_{n+1} = \frac{1}{2}\left(\boldsymbol{1} - \overline{\boldsymbol{b}}^{-1}_{n+1}\right)$, $\overline{\boldsymbol{b}}_{n+1} = \overline{\boldsymbol{F}}_{n+1}\overline{\boldsymbol{F}}^T_{n+1}$
11. Hencky strain by rate-form deformation gradient: $\overline{\boldsymbol{e}}^H_{n+1} = ln\sqrt{\overline{\boldsymbol{b}}_{n+1}}$

where $\overline{\nabla(\boldsymbol{u})}$ will be calculated following Bagi's method in Eq. (1), $\frac{\overline{\partial \boldsymbol{u}}}{\partial \boldsymbol{x}}$ is calculated with respect to coordinates in the current configuration, and $\frac{\overline{\partial \boldsymbol{u}}}{\partial \boldsymbol{X}}$ is calculated with respect to coordinates in the reference configuration, by Eqs. (12) and (7), respectively. Note that $\overline{\nabla(\boldsymbol{u})}$ is calculated from Eq. (1), while $\frac{\overline{\partial \boldsymbol{u}}}{\partial \boldsymbol{x}}$ is calculated from Eq. (12), which are different from each other Eq. ((12) is valid for finite strain, while Eq. (1) is not valid for finite strain).

Two tests are now considered to check the validity of these strain measures (including the Bagi small strain tensor $\overline{\boldsymbol{\epsilon}}^{Bagi}$): (i) comparison with macro-wall-strain, and (ii) large rotation test of granular assembly.

3.2.1. Comparison with macro-wall-strain during triaxial compression

The first test of these strain formulations is to compare with the macro-wall-strain, since the granular strain is meant to link the macro-deformation of an assembly of particles to the displacements of individual particles. There are two types of macro-wall-strain to be compared with (continuing from strain definition 11 in the previous section):

12. nominal wall strain, $\epsilon^{nom} = \frac{\Delta L}{L_0} = \frac{d}{L_0}$, and
13. logarithmic wall strain, $\epsilon^{log} = ln\left(\frac{L}{L_0}\right), L = L_0 + d$,

where d is the axial displacement, L_0 is the initial distance between the walls, and L is the current distance between the walls. The triaxial compression of a 5 mm × 5 mm × 4 mm assembly of F-75 Quartz Ottawa sand grains has been analyzed with the parameters in Table 1, assuming Hertzian contact and Coulomb frictional sliding between ellipsoidal particles; refer to Table 2 for additional parameters used here and also for the quasi-static pile penetration example, and to Yan et al. (2010) for more discussion. The assembly contains 939 particles (i.e., $\Omega^{\text{sub-domain}} = \Omega^{\text{assembly}}$, Fig. 6). A confining pressure of 1000 Pa is applied on the four boundaries in the x_1 and x_2 directions. Top and bottom boundaries in the x_3 direction move inwards to compress the assembly at a rate of 7.0×10^{-3} m/s. No gravity is applied in the simulation. The time step for this triaxial compression simulation is 7.5×10^{-8} s, and the tessellation will be updated at every 7.5×10^{-5} s. The results of calculating the different strain values versus time are plotted in Figs. 7, 8.

In Fig. 7 the normal strain in the x_3 direction is negative, which implies compression, and in Fig. 8, the normal strain in the x_1 direction is positive, which implies extension (the x_2 result is similar to the x_1 result, and thus is not shown). This is expected since the sub-domain/assembly is being compressed along the x_3 direction, allowing dilatation to occur in the x_1 and x_2 directions to

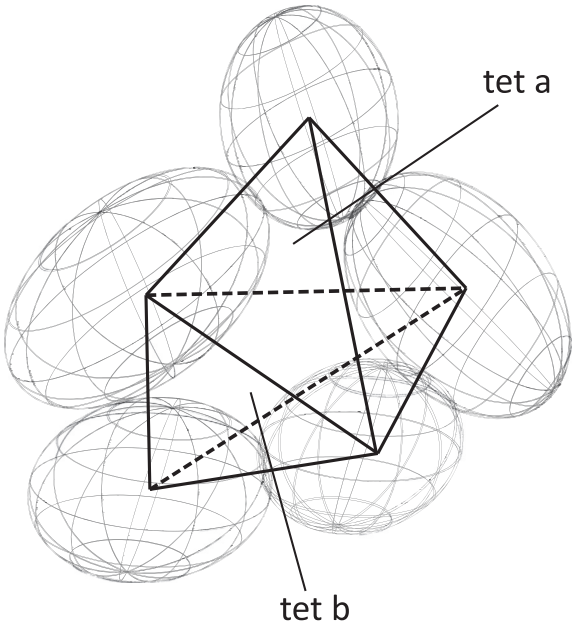

Fig. 4. A two *tet* assembly to show the difference between the *total quadratic term definition* and the *individual average definition*.

maintain the confining pressure. The values calculated from the different strain measures are within the same order of magnitude, i.e., there is no noticeable error in the small strain or finite strain measures for triaxial compression except for their differences due to geometric nonlinearity. For compressive strain in the x_3 direction, the rate strain $\bar{e}_{33,n+1}$ exhibits the largest value. The two macro-wall-strains in the x_3 direction can be calculated. Change of height of the assembly is $\Delta L = \left(1.0\times10^{6}\ steps\right)\times\left(7.5\times10^{-8}s\right)\times\left(-7.0\times10^{-3}\mathrm{m/s}\right) = -1.05$ mm, then $\epsilon^{nom} = \frac{\Delta L}{L_0} = \frac{-1.05}{4} = -0.2625$ and $\epsilon^{log} = ln\left(\frac{L}{L_0}\right) = ln\left(\frac{4-1.05}{4}\right) = -0.304$. These are the final values of the two macro-wall-strains in Fig. 7. For normal strain in the x_3 direction in Fig. 7, we can see that these Eulerian strain measures are close to the macro-wall-strains when the strain value is less than $|-0.15|$, which is the maximum strain value in Fig. 8. After that, $\bar{\boldsymbol{e}}_{n+1}$ becomes larger than the other strain measures. The *Eulerian strain by rate-form* is the same as *Eulerian strain by rate-form deformation gradient* as shown in Figs. 7 and 8. This is because both strains are based upon the spatial velocity gradient $\bar{\boldsymbol{l}}$ at time t_{n+1}. We will see that the four rate-form strains (*Eulerian strain by rate-form, Eulerian strain by rate-form deformation gradient, Lagrangian strain by rate-form deformation gradient*, and *Hencky strain by rate-form deformation gradient*) are the best strain measures among the seven strain measures presented in the paper because of the interval nature of their calculation over *calculation time interval* Δt, which will be concluded in Sections 4.1 and 4.2.

3.2.2. Large rotation test

For triaxial compression, the various strain measures lead to different values calculated due to geometric nonlinearity, although all within the same order of magnitude, i.e., they can be mapped with respect to each other through the deformation gradient (except for the linear strain measures). To further test and compare these strain measures for granular materials, we consider a rotation test to check if the finite strain formulations are invariant with respect to rigid body rotation. Consider a rigid body rotation whose motion is written as,

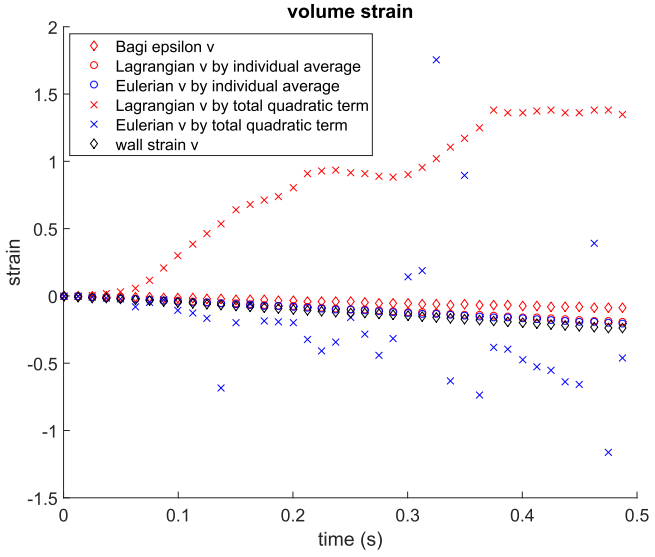

Fig. 5. Isotropic compression of an assembly with 52 F-75 Quartz Ottawa sand grains. Volumetric strain based upon linear Bagi strain, finite Lagrangian and Eulerian strains based upon *total quadratic term definition*, and finite Lagrangian and Eulerian strains based upon *individual average definition*, with comparison to nominal macro-wall-strain.

Table 1
Parameters used in the triaxial compression of a 5 mm × 5 mm × 4 mm assembly of F-75 Quartz Ottawa sand grains.

Time step Δt^{DEM}	1×10^{-7} s
Compression rate of boundary	7.0×10^{-3} m/s
Friction between particles	0.08
Background damping	$2/\Delta t^{DEM}$

Table 2
Parameters used in cavity expansion (Section 4.1) and and pile penetration (Section 4.2) examples.

	Cavity expansion, Section 4.1	Pile penetration, Section 4.2
Time step Δt^{DEM} (s)	5.0×10^{-7}	5.0×10^{-6}
Mass scale	1.0	10.0
Moment scale	1.0	10.0
Gravity scale (in negative x_3 direction)	1.0	1000.0
Background damping	0	4×10^{5}
Normal contact damping ratio	0.30	0.05
Friction between particles	0.50	0.50
Friction between particles and boundaries	0.50	0.50
Particle Young's modulus (E) (GPa)	29	29
Particle Poisson's ratio (ν)	0.25	0.25
Particle density (g/cm^3)	2.65	2.65

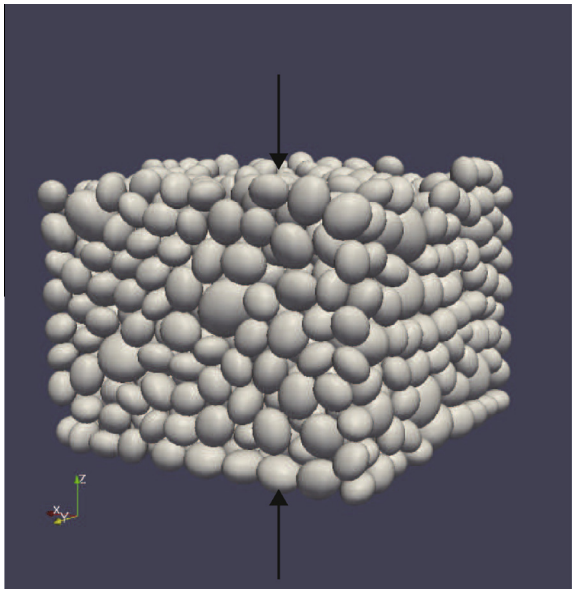

Fig. 6. Triaxial compression of a 5 mm × 5 mm × 4 mm assembly of F-75 Quartz Ottawa sand grains.

$$\boldsymbol{x} = \boldsymbol{Q}\boldsymbol{X} \tag{30}$$

where $\boldsymbol{Q}$ is a proper orthogonal tensor. Then, the deformation gradient tensor for this motion will be

$$\boldsymbol{F} = \boldsymbol{Q} \Rightarrow \frac{\partial \boldsymbol{u}}{\partial \boldsymbol{X}} = \boldsymbol{Q} - \mathbf{I} \tag{31}$$

The linear Lagrangian strain tensor for this motion is then calculated as,

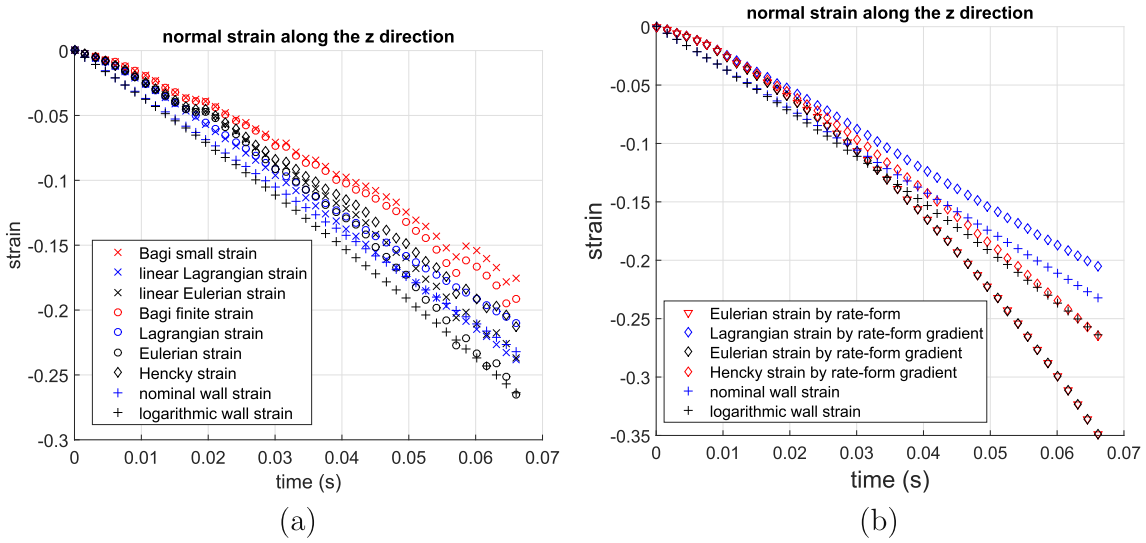

Fig. 7. Normal strain along x_3 direction for comparison between granular strain measures and macro-wall-strain: (a) *direct* strain compared to wall strains; (b) *rate* strain compared to wall strains.

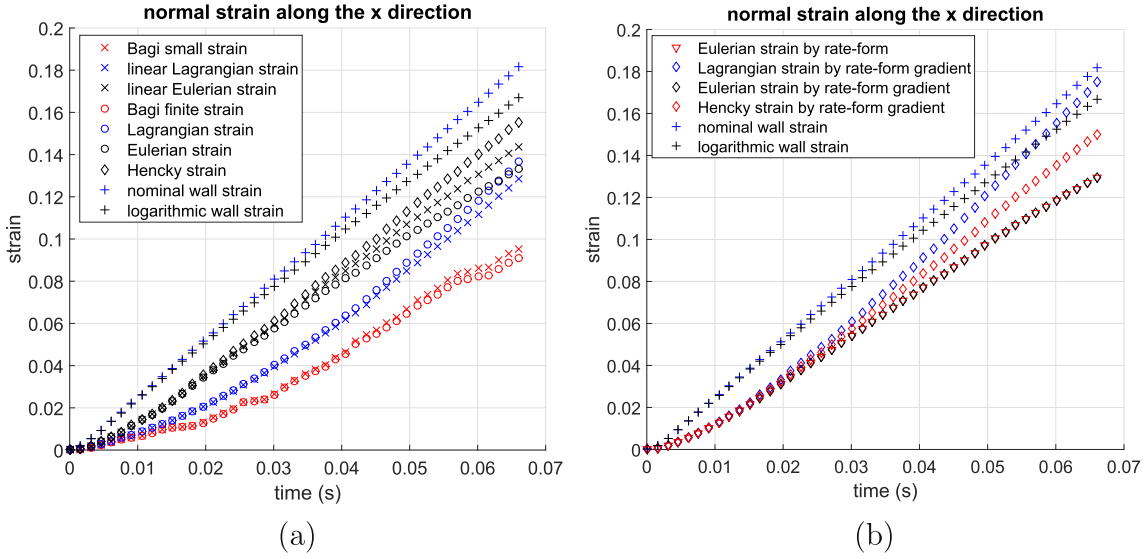

Fig. 8. Normal strain along x_1 direction for comparison between granular strain measures and macro-wall-strain: (a) *direct* strain compared to wall strains; (b) *rate* strain compared to wall strains.

$$\boldsymbol{E}^{lin} = \frac{1}{2}\left[\left(\frac{\partial \boldsymbol{u}}{\partial \boldsymbol{X}}\right) + \left(\frac{\partial \boldsymbol{u}}{\partial \boldsymbol{X}}\right)^T\right] = \frac{1}{2}\left[(\boldsymbol{Q}-\boldsymbol{I}) + (\boldsymbol{Q}-\boldsymbol{I})^T\right] = \frac{1}{2}\left(\boldsymbol{Q}+\boldsymbol{Q}^T-2\boldsymbol{I}\right) \tag{32}$$

which will not be $\boldsymbol{0}$ for large values of $\boldsymbol{Q}$. The finite Lagrangian strain tensor for this motion is,

$$\boldsymbol{E} = \frac{1}{2}\left[\left(\frac{\partial \boldsymbol{u}}{\partial \boldsymbol{X}}\right) + \left(\frac{\partial \boldsymbol{u}}{\partial \boldsymbol{X}}\right)^T + \left(\frac{\partial \boldsymbol{u}}{\partial \boldsymbol{X}}\right)^T\left(\frac{\partial \boldsymbol{u}}{\partial \boldsymbol{X}}\right)\right] = \frac{1}{2}\left[(\boldsymbol{Q}-\boldsymbol{I}) + (\boldsymbol{Q}-\boldsymbol{I})^T + (\boldsymbol{Q}-\boldsymbol{I})^T(\boldsymbol{Q}-\boldsymbol{I})\right] = \frac{1}{2}\left(\boldsymbol{Q}^T\boldsymbol{Q}-\boldsymbol{I}\right) = \boldsymbol{0} \tag{33}$$

which is independent of large rotation $\boldsymbol{Q}$. This result also holds for Eulerian strain $\boldsymbol{e}$, rate-form strains, and Hencky strain $\boldsymbol{e}^H$. Thus, the finite strain measures should not be influenced by a rigid body rotation of the whole particle assembly. An analytical proof of invariance with respect to rigid body rotation is provided in Appendix B, and a numerical example is provided next.

3.2.3. Numerical results of large rotation test

The 5 mm × 5 mm × 4 mm F-75 Quartz Ottawa sand sub-domain/assembly (i.e., $\Omega^{\text{sub-domain}} = \Omega^{\text{assembly}}$) will be used to test if the numerical results of granular Lagrangian strain and granular Eulerian strain will always be zero during a large rigid body rotation. In this rotation test, all the particles in the assembly will be applied the same rotation tensor. Specifically, this assembly will be rotated along x_1, x_2 and x_3 directions at the same time by and angle $\frac{\pi}{2}$ as shown in Figs. 9–14.

Two different simulations are conducted: one without updating the tessellation, and the other one with an update of the tessellation at every 1×10^{-3} radians of rotation. Both provide exactly

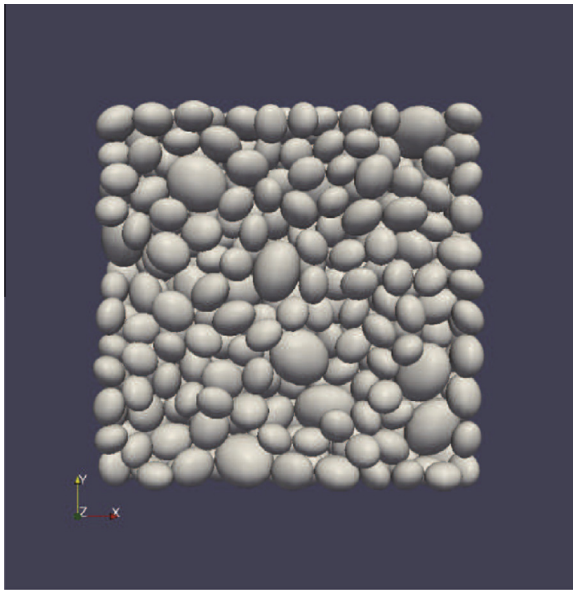

Fig. 9. Initial snapshot when rotation angle is 0° along x_1, x_2 and x_3 directions.

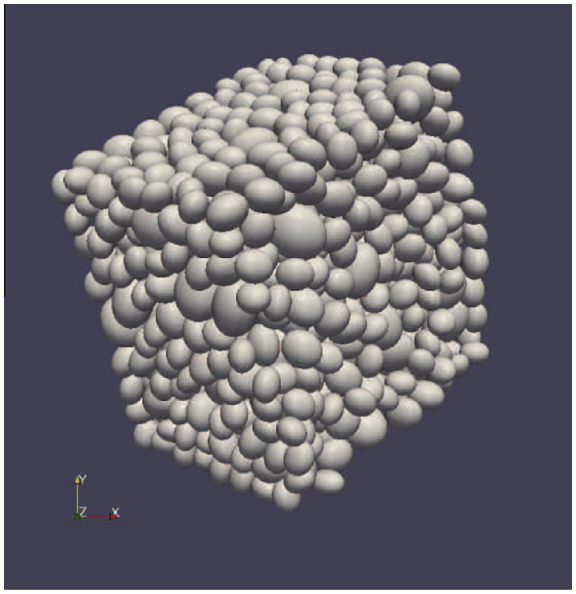

Fig. 11. Snapshot when rotation angle is 36° along x_1, x_2 and x_3 directions.

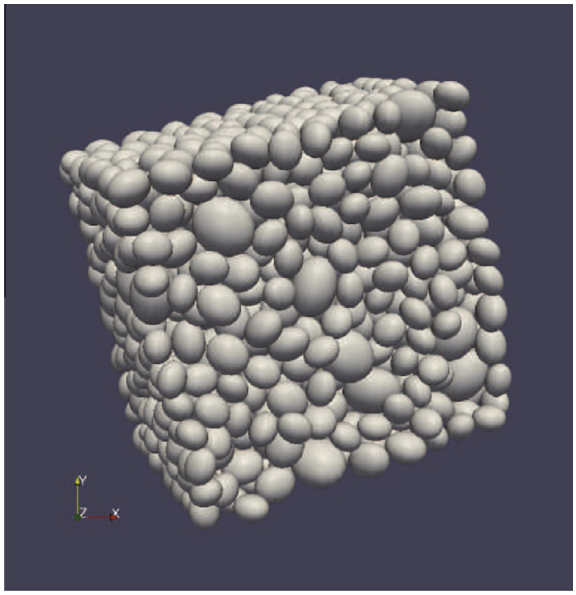

Fig. 10. Snapshot when rotation angle is 18° along x_1, x_2 and x_3 directions.

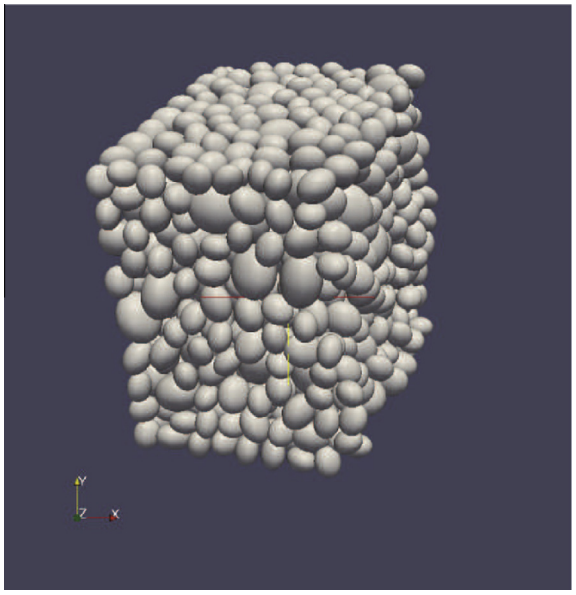

Fig. 12. Snapshot when rotation angle is 54° along x_1, x_2 and x_3 directions.

the same result because the particles do not have relative displacements during rigid body rotation.

The volumetric finite Bagi strain $\overline{\epsilon}_v^{Bagi,finite} = \overline{\epsilon}_{11} + \overline{\epsilon}_{22} + \overline{\epsilon}_{33}$ is shown to be ≈ -4000 at the end of rotation. Bagi's volumetric small strain is shown to be ≈ -80 at the end of rotation. Eulerian volumetric strain and Lagrangian volumetric strain are shown to be $\approx 1 \times 10^{-12}$, rate-form Eulerian granular strain is $\approx 1 \times 10^{-3}$, Hencky volumetric strain is $\approx 1 \times 10^{-8}$, and the Jacobian of deformation $\bar{J}$ is exactly =1. The result shows that the average spatial velocity gradient $\bar{\boldsymbol{l}} = \mathbf{0}$, which is expected since no relative displacements between particles occur during the rotation. Then the three volumetric strains by rate-form deformation gradient are also =0. The volumetric strains of the Lagrangian formulation, Eulerian formulation, linear Lagrangian formulation, linear Eulerian formulation, Eulerian strain by rate-form, Hencky strain, and Jacobian of deformation are plotted against the rotation angle in Fig. 15.

The numerical results provided in Fig. 15, together with the analysis in the above section, demonstrate that the granular Lagrangian strain, granular Eulerian strain, granular strains by rate-form, and granular Hencky strain can pass the large rotation test, meaning these seven granular strains are independent of rigid body rotation, and they are indeed finite strain measures (as is to be expected based upon their formulations within nonlinear continuum mechanics). Combined with comparison to the macro-wall-strain calculations, these strain measures have passed the two initial validity tests. We now present more complex

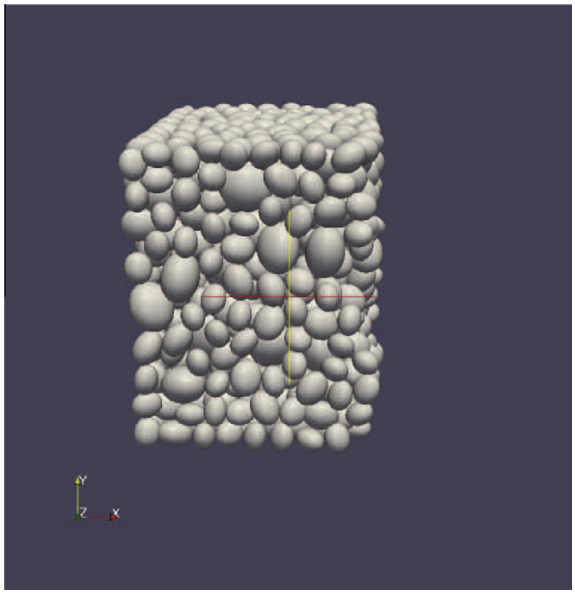

Fig. 13. Snapshot when rotation angle is 72° along x_1, x_2 and x_3 directions.

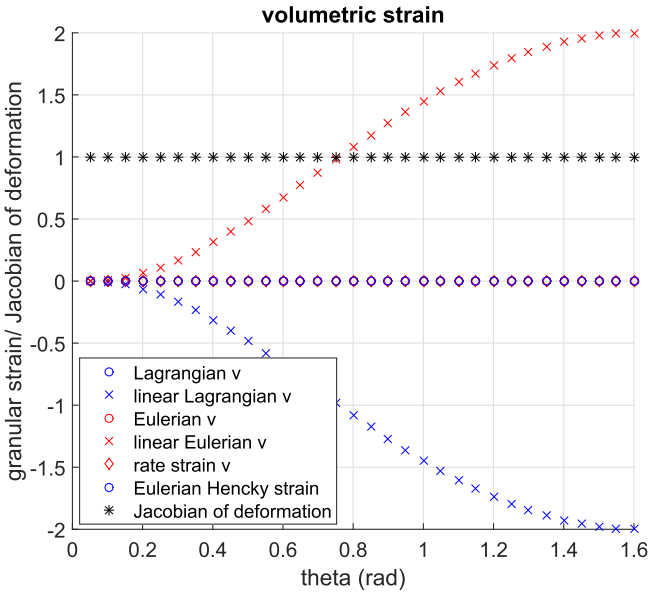

Fig. 15. Plot of volumetric strains for large rotation test.

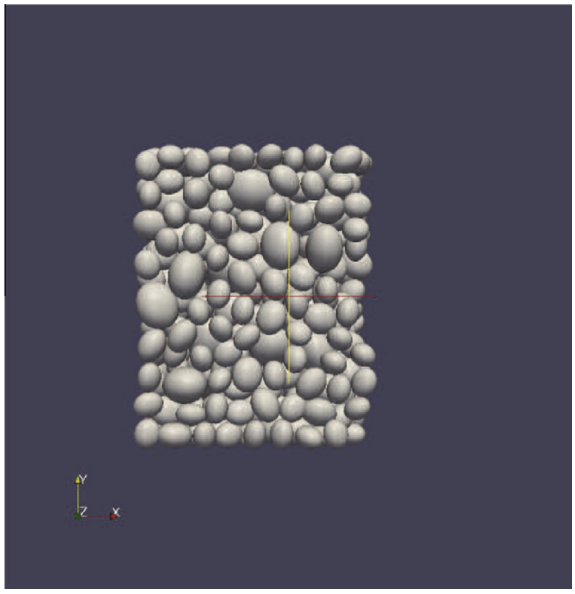

Fig. 14. Snapshot when rotation angle is 90° along x_1, x_2 and x_3 directions.

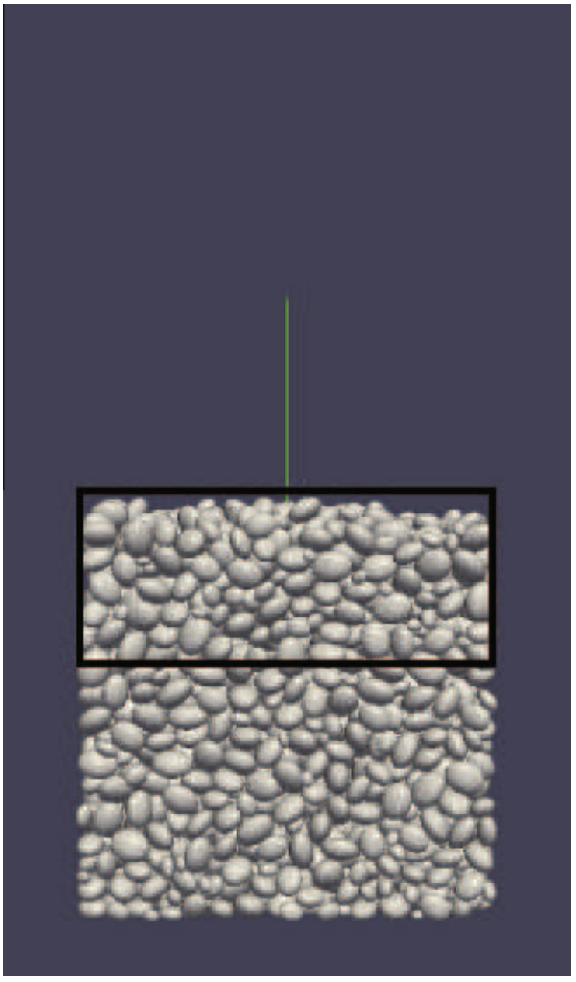

Fig. 16. Snapshot at 0.000 s.

numerical examples at large deformation to further test these granular finite strain measures.

4. Numerical examples

In this section, two numerical simulations demonstrating finite strains will be conducted using Ellip3D (Yan et al., 2010), and their stresses and strains will be plotted: one example is cavity expansion (dynamic simulation), and the other is pile penetration (quasi-static simulation). Ellip3D is a C++ Discrete Element Method (DEM) code, in which ellipsoids are used to simulate the soil particles with parameters in Table 2. For more discussion of the DEM parameters, refer to Yan et al. (2010). For example, the mass, moment, and gravity scaling parameters are set to 1.0 for the cavity expansion dynamic simulation, and set to values greater than 1.0 to mimic a quasi-static simulation for pile penetration, using the concept of dynamic relaxation (Underwood, 1983). Background damping is mass proportional damping, and is 0 for dynamic simulations, and a large value for quasi-static simulations.

Fig. 17. Snapshot at 0.075 s.

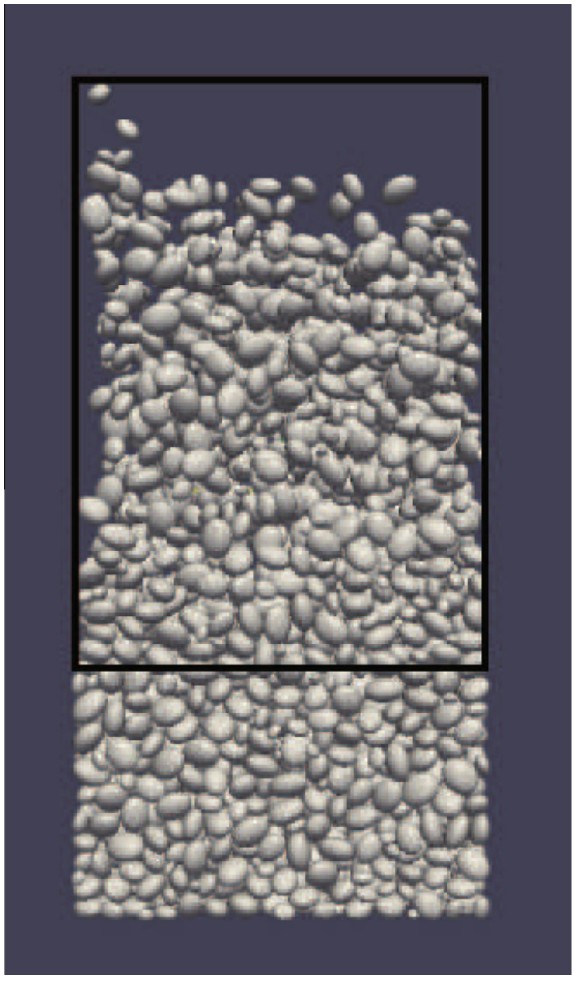

Fig. 18. Snapshot at 0.113 s.

Invariants of stress and strain will be used to plot results during the large deformation simulations. The definitions of these invariants are introduced:

1. *Eulerian octahedral shear strain*, which can also be Hencky strain $\overline{\boldsymbol{e}}^{H}$ (both direct, or rate-based):

$$\overline{\gamma}^2_{oct} = \frac{1}{9}\left[(\overline{e}_{11}-\overline{e}_{22})^2+(\overline{e}_{11}-\overline{e}_{33})^2+(\overline{e}_{22}-\overline{e}_{33})^2\right] + \frac{2}{3}\left[\overline{e}^2_{12}+\overline{e}^2_{13}+\overline{e}^2_{23}\right]$$

2. *Lagrangian octahedral shear strain* (direct, or rate-based):

$$\overline{\Gamma}^2_{oct} = \frac{1}{9}\left[(\overline{E}_{11}-\overline{E}_{22})^2+(\overline{E}_{11}-\overline{E}_{33})^2+(\overline{E}_{22}-\overline{E}_{33})^2\right] + \frac{2}{3}\left[\overline{E}^2_{12}+\overline{E}^2_{13}+\overline{E}^2_{23}\right]$$

3. *Octahedral shear rate of deformation tensor* $\boldsymbol{d}$:

$$\overline{\gamma}^2_{oct,\boldsymbol{d}} = \frac{1}{9}\left[\left(\overline{d}_{11}-\overline{d}_{22}\right)^2+\left(\overline{d}_{11}-\overline{d}_{33}\right)^2+\left(\overline{d}_{22}-\overline{d}_{33}\right)^2\right] + \frac{2}{3}\left[\overline{d}^2_{12}+\overline{d}^2_{13}+\overline{d}^2_{23}\right]$$

4. *Eulerian and Lagrangian volumetric strains* (both direct, or rate-based), *volumetric rate of deformation tensor* $\boldsymbol{d}$, *Jacobian of deformation*:

$$\overline{E}_v = \overline{E}_{11}+\overline{E}_{22}+\overline{E}_{33}, \quad \overline{e}_v = \overline{e}_{11}+\overline{e}_{22}+\overline{e}_{33},$$
$$\overline{d}_v = \overline{d}_{11}+\overline{d}_{22}+\overline{d}_{33}, \quad \overline{J} = det\overline{\boldsymbol{F}}$$

5. *Cauchy octahedral shear stress*:

$$\overline{\tau}^2_{oct} = \frac{1}{9}\left[(\overline{\sigma}_{11}-\overline{\sigma}_{22})^2+(\overline{\sigma}_{11}-\overline{\sigma}_{33})^2+(\overline{\sigma}_{22}-\overline{\sigma}_{33})^2\right] + \frac{2}{3}\left[\overline{\sigma}^2_{12}+\overline{\sigma}^2_{13}+\overline{\sigma}^2_{23}\right]$$

6. *Cauchy mean stress*:

$$\overline{\sigma}_{mean} = \frac{1}{3}(\overline{\sigma}_{11}+\overline{\sigma}_{22}+\overline{\sigma}_{33})$$

4.1. Cavity expansion

The cavity expansion simulation will take place within a boxed assembly of particles, which has boundaries in the x_1 and x_2 directions and bottom boundary in the x_3 direction but no top boundary allowing free expansion vertically (see Figs. 16–21, where the black box indicates the moving sub-domain $\Omega^{\text{sub-domain}}$, and the green lines are the axes in ParaView visualization package). The dimensions of the box are 0.05 m × 0.05 m × 0.05 m. The box contains 4050 ellipsoidal particles with $D_{50} = 1.8$ mm (i.e., diameter of particle, 50% of which are smaller). The center of the box is the coordinate origin, the center of the cavity is at $(0, 0, -0.0125\ \text{m})$, and the dimension of the cavity is 0.05 times the box size. At first,

the radius of the particles within the cavity will be increased by 0.4 times such that the contact forces between these expanded particles will be very large, leading to the initial cavity expansion effect. Particles will then separate, fly up, and settle again by gravity. The tessellation is updated at every 2.5×10^{-3} *s*, while the simulation lasts 375×10^{-3} *s*. For the granular strains by rate-form, the *calculation time interval* Δt is every 1000 time steps which leads to $\Delta t = 5 \times 10^{-4}$ s; note that Δt is *not* the time step used in the central difference in time integration of the balance of linear and angular momentum equations in the DEM simulation (see Table 2 for this time step). Figs. 16–21 are snapshots of the cavity expansion simulation.

Volumetric stress and strain for the particle assembly during cavity expansion may be calculated in two ways: (1) take the volume average over the total assembly (i.e., calculate granular stress and strain within the total spatial domain, such that $\Omega^{\text{sub-domain}} = \Omega^{\text{assembly}}$), or (2) use a sub-domain to calculate the granular stress and strain ($\Omega^{\text{sub-domain}} \subset \Omega^{\text{assembly}}$). From these snapshots of the cavity expansion, Figs. 16–21, it is apparent that particles outside of (i.e., below) the sub-domain may not move significantly, such that only particles within the sub-domain may experience large deformation. The volumetric stress and strain are then calculated within this sub-domain. The results from the two different sub-domains (one is the total assembly of particles $\Omega^{\text{sub-domain}} = \Omega^{\text{assembly}}$, and the other is the sub-domain shown varying with time following the top layer of separating particles in Figs. 16–21, $\Omega^{\text{sub-domain}} \subset \Omega^{\text{assembly}}$) are compared with each other.

4.1.1. Stress and strain within the total assembly: $\Omega^{\text{sub-domain}} = \Omega^{\text{assembly}}$

In Fig. 22(a), for $t < 0.01$ s, all of the various finite strain measures are nearly equal. Then, as the particles separate and the assembly expands, the differences between the various strain measures become larger. Finally, the strain measures reach steady-state as the particles in the assembly come to rest under gravity. When comparing the various strain measures, there are noticeable differences between them for $t > 0.03$ s. This is to be expected because under large deformation, the particles fly up and separate, leading to significant nonlinear geometric terms that will make the calculation of the strains (Lagrangian, Eulerian, and Hencky) different. Recall that there are two general approaches to calculating finite strain in the paper based upon the Delaunay tessellation and linear tetrahedral shape function interpolations: (1) *direct* calculation based upon interpolation of particle centroid displacements, and (2) *rate-form* calculation based upon semi-implicit time integration of the average, interpolated, velocity gradient $\bar{\boldsymbol{l}}_{n+1}$ (from which the integrated rate-form deformation gradient at time $t_{n+1}, \bar{\boldsymbol{F}}_{n+1}$ is calculated). We see in Fig. 22(a), the volumetric granular strains by *rate-form* are generally smoother than the *direct* granular strains, and they return to near zero

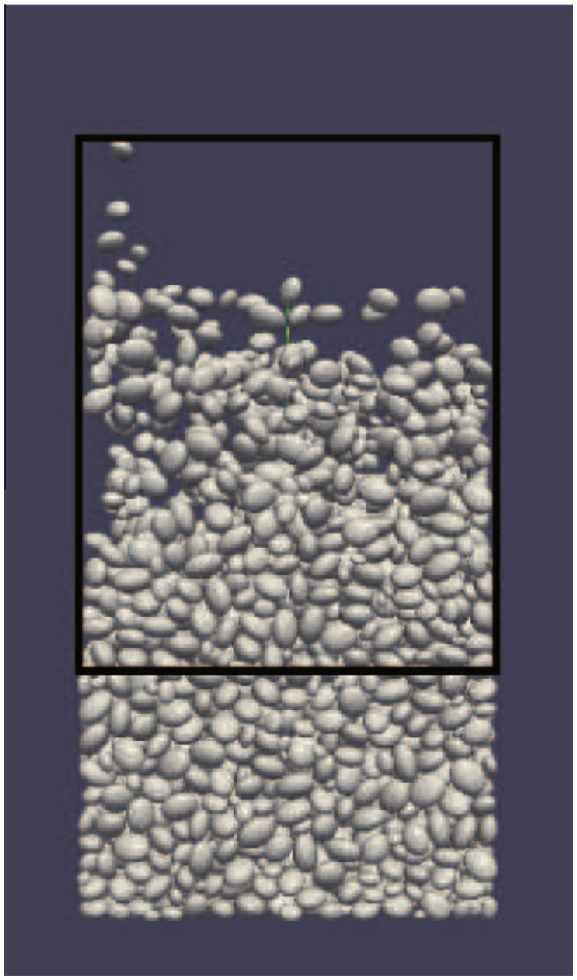

Fig. 19. Snapshot at 0.150 s.

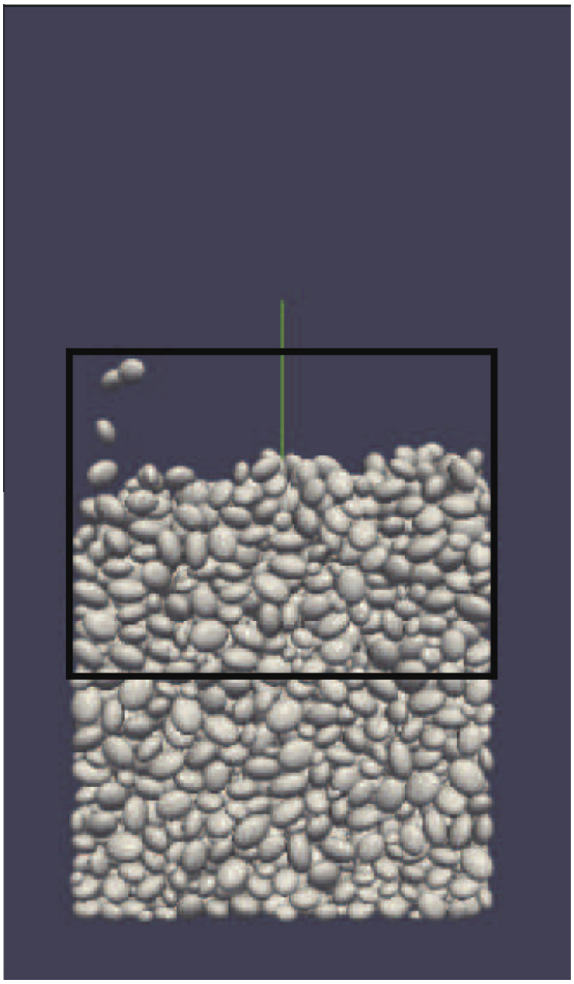

Fig. 20. Snapshot at 0.188 s.

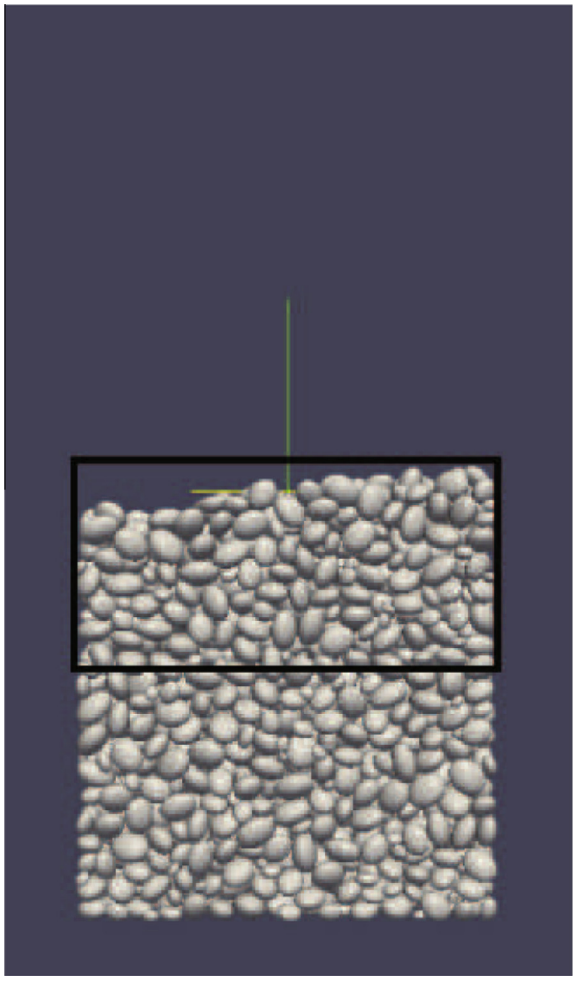

Fig. 21. Snapshot at 0.375 s.

permanent volumetric strain at the end of the simulation. The initial and final volumes of the assembly can be calculated by summation over all the tetrahedral elements in the initial and final tessellations. The initial volume is $V = 111,601$ mm^3, and final volume is $v = 113,598$ mm^3. Then, in terms of predicting steady-state volumetric strain, the granular strains by rate-form can be trusted to represent properly the deformation of the expansion simulation because of the small amount of steady-state volumetric strain observed, such as, nominally $(|v - V|/V) = (113,598 - 111,601/111,601) = 0.018$ or 1.8% ; $|v - V|/V$ is plotted in Fig. 22(a) as *ratio of expanded volume*. What is the reason for this? It is because the *direct* granular Lagrangian and Eulerian strains $\overline{\boldsymbol{E}}$ and $\overline{\boldsymbol{e}}$, respectively, are defined based upon total particle centroid displacement vectors $\boldsymbol{u}$ at the current time. For complex large deformation particle-scale response such as cavity expansion, the particle displacement vectors are large as particles cross each other's motion paths. The granular strains by rate-form, however, are based upon the velocity gradient $\overline{\boldsymbol{l}}_{n+1}$ (and integrated deformation gradient $\overline{\boldsymbol{F}}_{n+1}$) always evaluated with respect to the particle centroid for each chosen *calculation time interval* Δt. Thus, this interval strain-rate calculation, based upon current tessellation and rate is more true to the actual deformation.

It is apparent that there are three different phases during the expansion simulation which can be observed from the strains in Fig. 22: (i) From 0 to 0.1 s, the particles in the assembly separate and fly up. The snapshots of the simulation, Figs. 16–18, also show this expansion. During this phase, the strain increases very quickly. (ii) From 0.1 to 0.2 s, the particles in the assembly deposit again under gravity (snapshots in Figs. 19 and 20). During this process, the strain decreases. (iii) After 0.2 s, the particle assembly is at near rest (snapshot in Fig. 21). The strain during this process should reach steady-state (Fig. 22(a)).

Since the initial expansive force is large, the mean stress for the particle assembly at the first time step is $\approx -1.4 \times 10^4$ Pa. The stress plot figure (Fig. 22(b)) is thus plotted after the third time step. This will be avoided in the next section, when calculating the stress and strain within the sub-domain volume, because the initial expansive force is a result of the increased contact forces of the cavity particles, while these cavity particles are beyond the sub-domain (black outlined box) in Figs. 16–21. Thus, these extremely large contact forces will not be considered in the stress calculation within the sub-domain in Section 4.1.2.

The mean Cauchy stress of the assembly during the expansion simulation (Fig. 22(b)) is negative under compression due to gravity. Since at the initiation of loading, the radius of the cavity particles are increased by 0.4 times, these cavity particles will overlap each other and their neighboring particles, which will produce large initial repulsive contact forces between these particles, and in turn, large initial particle centroid velocities. As many particles separate and rise, there will be fewer contacts between particles, leading to a very quick decrease of the Cauchy stress tensor $\overline{\sigma}_{ij}$, and in turn the mean stress (Fig. 22(b)). In this section, the stress is calculated over the total assembly, and since many particles do not separate, this will not show clearly the three different phases of the expansion simulation in the stress figure (Fig. 22(b)). It will be shown in the next section that the three different phases are more noticeable in the stress plot for the sub-domain calculation (Fig. 23(b)). The steady-state final phase, however, is still clear in the stress calculation in Fig. 22(b). After 0.2 s, the mean stress (Fig. 22(b)) approaches its steady-state value (negative in compression for mean stress).

4.1.2. Stress and strain within the sub-domain: $\Omega^{\text{sub-domain}} \subset \Omega^{\text{assembly}}$

It was written in the previous section that many particles in the total assembly do not translate or rotate enough to cause a large deformation during the cavity expansion simulation; these are the particles below the separating particles. Thus, calculation of stress and strain can be performed within the sub-domain (black box) in Figs. 16–21. The sub-domain consists of all the particles above the bottom of the sub-domain, in which the stress and strain for these particles will be calculated. The bottom of the sub-domain is fixed during the simulation. In this example, the distance between the bottom of the sub-domain and the bottom of the container is 0.6× the height of the initial assembly. As mentioned in the previous section, the initially expanding cavity particles are not within this sub-domain. One can calculate the stress and strain at any point of the assembly with the help of defined sub-domains (also known as, RVEs; depending on if there are enough particles to warrant a continuum approximation; the number of particles in this sub-domain is ≈2000).

We compare plots in this section with their corresponding plots in the previous section, namely Fig. 23 with Fig. 22. It is observed that the strain magnitudes within the sub-domain are larger than those within the total assembly because the averaging domain volume is smaller, yet the motion of the particles is the same.

It was mentioned in the previous section that the stress plot for the total assembly (Fig. 22(b)) cannot show the three different phases of cavity expansion simulation (separating and flying up, settling under gravity, and steady-state at rest), while that within the sub-domain (Fig. 23(b)) can show clearly the three different phases. In Fig. 23(b), at the beginning, stresses are very large because of the initial cavity expansion loading. From 0 to 0.1 s

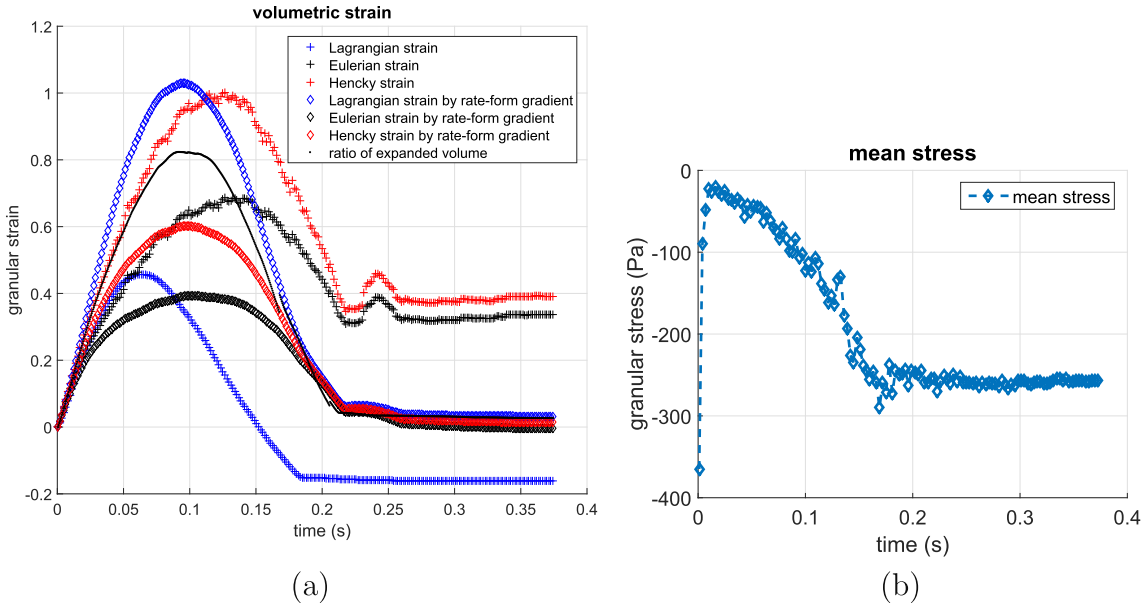

Fig. 22. Cavity expansion simulation for $\Omega^{\text{sub-domain}} = \Omega^{\text{assembly}}$: (a) volumetric strain versus simulation time; (b) mean stress versus simulation time.

(snapshots in Figs. 16–18), almost all the particles in the sub-domain are separating, thus many particles will lose their contacts with each other very quickly, as shown in Figs. 17 and 18, which will cause the stresses to decrease quickly. Then there will be a short period (about $0.03 < t < 0.07$ s in Fig. 23(b)) that the contacts are disappearing in the sub-domain, and the stresses will be nearly zero within this period. From 0.1 to 0.2 s (snapshots in Figs. 19 and 20), particles are depositing under gravity after they reach their peaks. More and more particles will re-contact with each other, leading to increasing stresses during this period. After 0.2 s, particles in the assembly come to rest under gravity, leading to a stable steady-state stress state. The corresponding volumetric stress–strain plot is shown in Fig. 24. The oscillations in the mean stress values are due to particles coming in and out of contact (i.e., colliding) as they deposit under gravity, after reaching their maximum height (and separation distances) at zero stress state. For further interpretation of the mean stress versus volumetric strain curves in Fig. 24 for cavity expansion simulation, we consider the beginning of loading at the lower left portions of the curves, which correspond to near zero volumetric strain under static gravity loading (negative stress in compression). As the cavity expands and pushes dynamically the particles upward, separating them as they fly vertically, the mean stress (same for each curve, given there is only one stress definition in the current configuration, but multiple strain definitions) decreases to zero (i.e., becomes less negative until it reaches zero). This near zero mean stress state for the four curves indicates that few particles are in contact. For the four curves, as the particles continue to separate and fly vertically, volumetric strain (positive in expansion) increases (with values depending on the finite strain measure used, in this case all in the current deformed configuration). Because of gravity loading in the $-x_3$ direction, the particles begin to settle again at

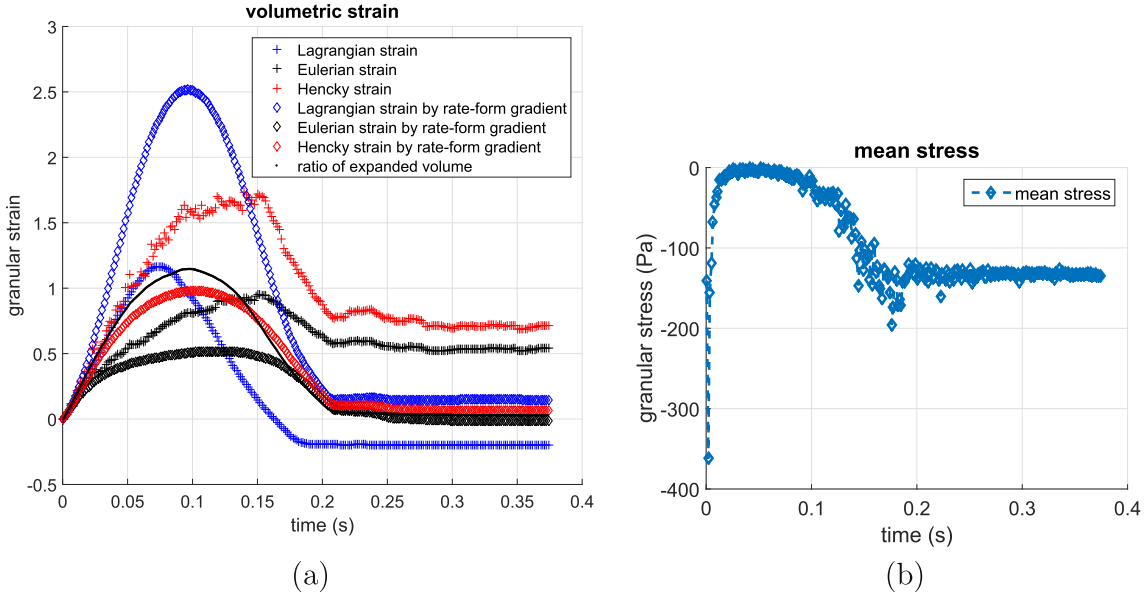

Fig. 23. Cavity expansion simulation for $\Omega^{\text{sub-domain}} \subset \Omega^{\text{assembly}}$: (a) volumetric strain versus simulation time; (b) mean stress versus simulation time.

approximately the maximum volumetric strain, and thus the mean stress becomes more negative as the volumetric strain decreases. The purpose of the comparison of these four curves is to show that the rate-form strains more realistically predict near zero residual volumetric strain (compare Figs. 16 and 21), whereas the two non-rate-form curves predict artificial residual volumetric strain (≈0.75 for granular Hencky strain, and ≈0.5 for granular Eulerian strain), thus confirming that the rate-form finite strain measures are the proper ones to use for interpreting discrete element simulation results.

4.2. Pile penetration

For the pile penetration example (Yan et al., 2010), a large ellipsoidal particle is penetrated into a particle assembly with fixed spherical particles as its boundaries shown in Fig. 25(a). The three semi-principal-lengths of the pile particle are 60.0 mm,6.0 mm , and 6.0 mm. Radii of the spherical boundary particles are identical at 2.475 mm. The free particles are also identical, of which the semi-principal-lengths are 2.5 mm,2.0 mm, and 1.5 mm. The dimensions of the container in the x_1 and x_2 directions are −0.025 m to +0.025 m, and its height is −0.03 m to +0.06 m. The sub-domain in which we calculate the granular stress and strain is 0.03 m to 0.06 m in the x_3 direction, and from −0.015 m to +0.015 m in the x_1 and x_2 directions, as shown by the cross-hatched box in Fig. 25(b), and the black outlined box in Fig. 25(a). There are about 1200 boundary particles and 5000 free ellipsoidal particles in the assembly, while about 450 particles are in the sub-domain.

The tessellation is updated every 5×10^{-3} s, and the simulation lasts about 350×10^{-3} s. For the granular strains by rate-form, the *calculation time interval* Δt is 1000 time steps, which is $=5 \times 10^{-3}$ s. This simulation is controlled by the vertical displacement of the pile. The speed of the pile penetration is 0.25 m/s, constrained to be vertical (no lateral or rotational velocity). Within the particle sub-domain, the stresses and strains are plotted against pile penetration depth.

It is noticed that there is a significant difference between the granular Eulerian strains (*direct* and by *rate-form*) in Fig. 26. When the *granular Eulerian strain* is calculated, only current coordinates $\boldsymbol{x}$ are used in Eq. (11), while *granular Eulerian strain by rate-form* still involves the contribution from last strain calculation step, such as $\bar{\boldsymbol{e}}_n$ in Eq. (20). This leads to the difference between *granular Eulerian strain* and *granular Eulerian strain by rate-form* ; the rate-form strain is thus more smoothly varying over time. This difference is a result of the particles inter-mixing (i.e., crossing paths) within the sub-domain, which the rate-form accounts for, but the direct calculation of strain does not in a smooth way. The volumetric granular strains by rate-form (Fig. 26(a)) can reach ≈0.2, which is a relatively large deformation. However, the octahedral shear strain is not as large (≈0.03, Fig. 26(b)). This is because there are many particles that rotate during pile penetration, while their translations are relatively small. At present, the strain measure formulations in the paper do not account for individual particle rotations, such that these particle rotations are not considered in the calculation of shear strain (as we would do for a micropolar theory (Kruyt, 2003)).

The volumetric and octahedral stress–strain plots are shown in Fig. 27. The mean stress and octahedral shear stress are increasing with penetration depth from 0.00 m to 0.03 m, and decreasing >0.03 m. This region corresponds to the x_3 dimension of the sub-domain as shown in Fig. 25(b). This is because as the pile penetrates deeper within the sub-domain, more particles in the sub-domain will be pushed outward by the pile, thus the contact forces between particles and pile will increase. These increasing contact forces between pile and the neighboring particles will be used to calculate the granular stress, as well as the contact forces amongst particles. The contact forces between particles and the pile are larger than those amongst the particles. Thus, the stress will increase within the sub-domain. As the tip of the pile penetrates beyond the sub-domain, there will be fewer particles in the sub-domain to be pushed out by the pile, thus the contact forces between the particles and pile will be smaller as the displaced particles adjust to their equilibrium positions. Then the stress will decrease. The mean stress (Fig. 27(a)) is negative which implies compression since the particles are pushed outward by the pile. We can also see clearly that the pile penetration involves two phases: pile tip penetrates (i) within and (ii) beyond the sub-domain. The authors note that eventually we will substitute a discrete numerical method (such as the Discrete Element

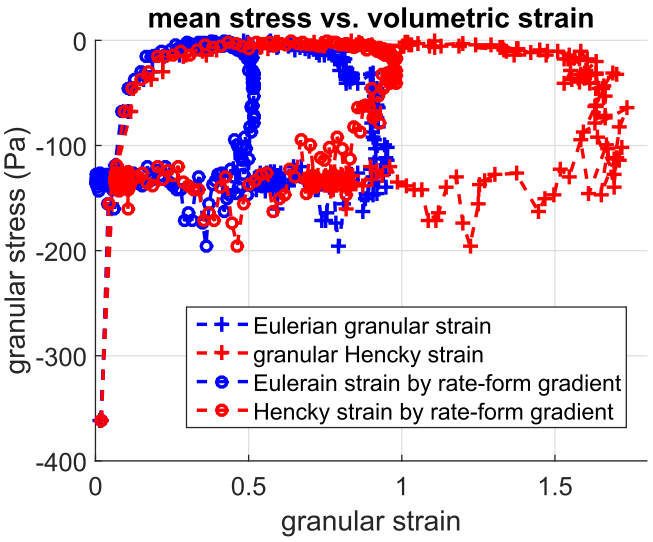

Fig. 24. Mean stress vs. volumetric strain for cavity expansion simulation with $\Omega^{\text{sub-domain}} \subset \Omega^{\text{assembly}}$.

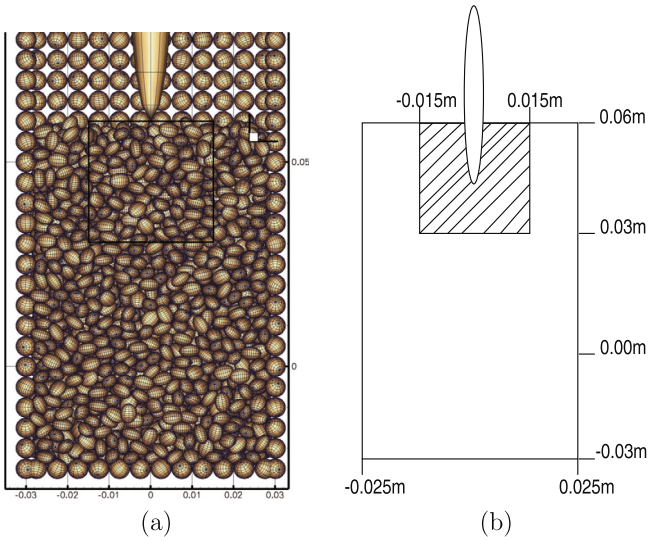

Fig. 25. (a) Initial state of assembly in pile penetration simulation, showing cross-section of plane of penetration; (b) cross-hatched sub-domain for granular stress and strain calculation in pile penetration simulation.

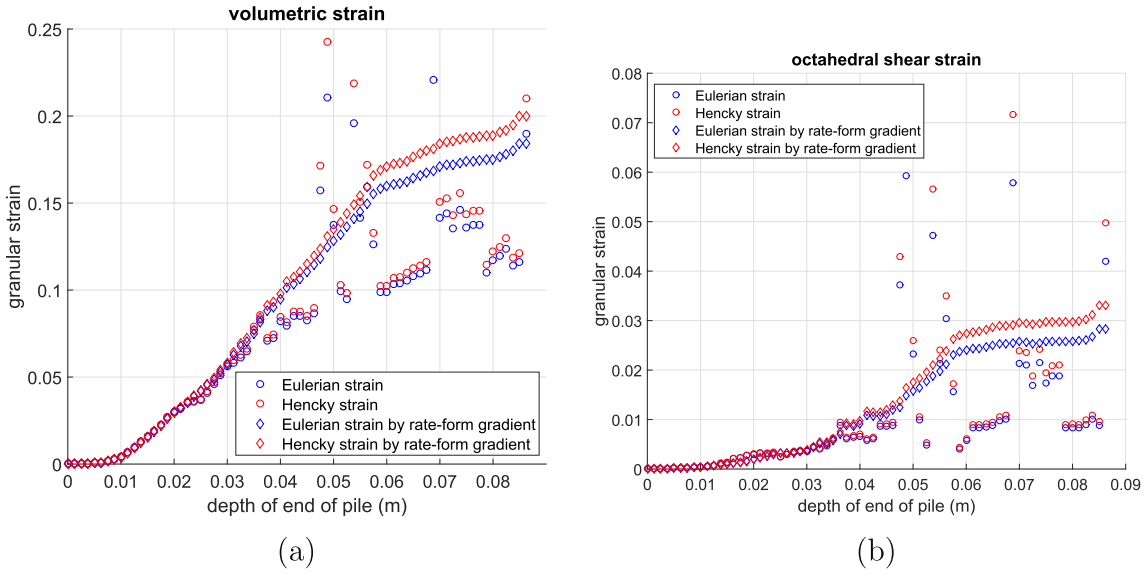

Fig. 26. (a) Volumetric strain versus depth of pile penetration. (b) Octahedral shear strain versus depth of pile penetration.

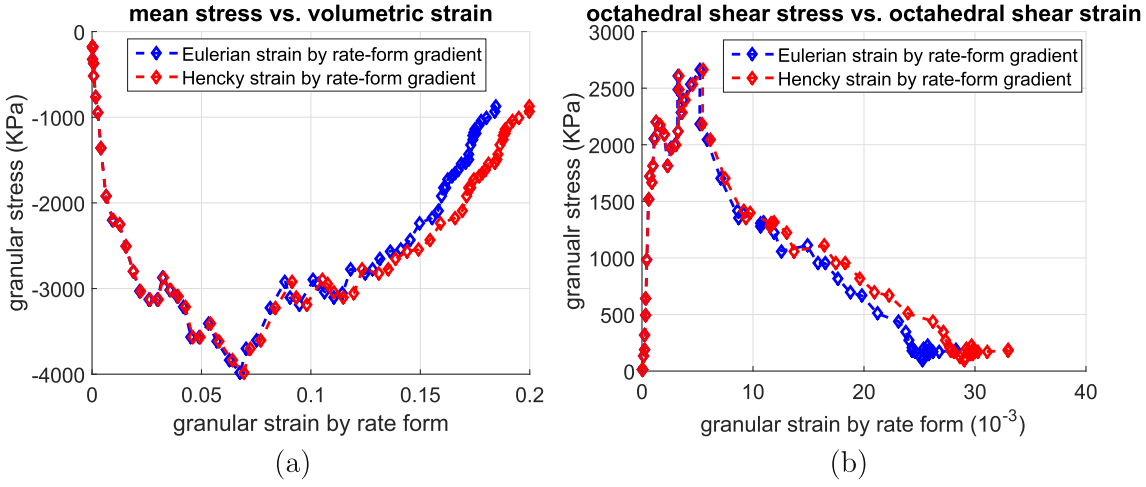

Fig. 27. (a) Mean stress vs. volumetric strain for pile penetration sub-domain. (b) Octahedral shear stress vs. octahedral shear strain for pile penetration sub-domain.

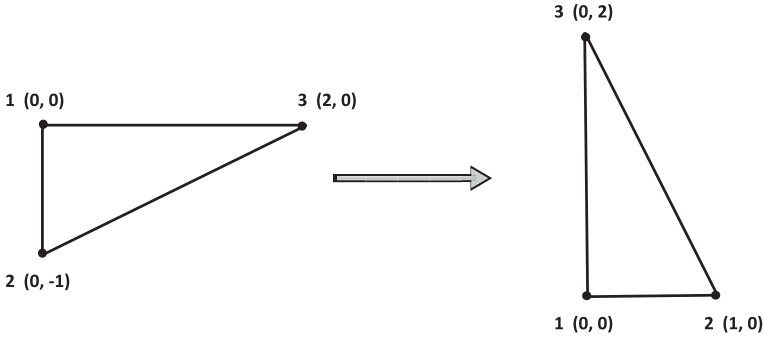

Fig. 28. Rotating a triangle in-the-plane.

Method (DEM) in this paper) in the region around the pile tip in lieu of a continuum approximation (Regueiro and Yan, 2011, 2013). However, there are many analysts who still prefer a continuum approximation (through an Arbitrary-Lagrangian–Eulerian (ALE) method, or meshless method like the Material Point Method (MPM) or Peridynamics) rather than maintaining a discrete representation at the pile tip (requiring adaptive computations to move this discrete particle representation with the

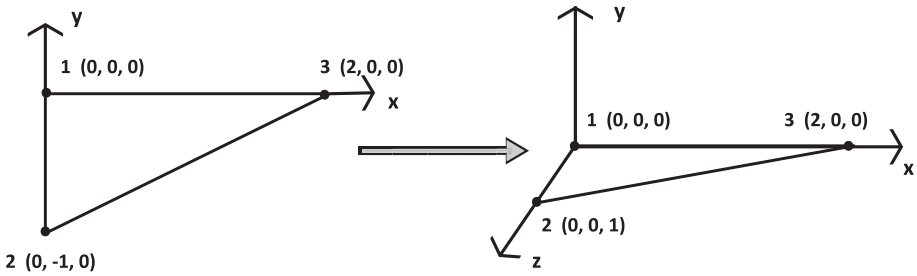

Fig. 29. Rotating a triangle out-of-the-plane.

moving pile tip). Thus, stress and (in this paper) strain calculations for general three-dimensional large deformational loading conditions are still of interest in these regions. The DEM simulations in this paper, and corresponding stress and strain calculations for large deformations, can be used to motivate these continuum constitutive model forms.

5. Conclusions

Seven finite strain measures for granular materials have been developed: (1) granular Lagrangian strain, (2) granular Eulerian strain, (3) granular Hencky strain, (4) granular Eulerian strain by rate-form, (5) granular Lagrangian strain by rate-form deformation gradient, (6) granular Eulerian strain by rate-form deformation gradient, and (7) granular Hencky strain by rate-form deformation gradient. It is shown that (4) and (6) are equivalent. The comparison of these strain measures, including Bagi's small strain measure (Bagi, 1996), with macro-wall-strains has shown that these granular finite strain measures calculate values close to expected macro-wall-strains (when using the *individual average definition* for the *direct* strain calculations). In summary, the finite strain measures have the following advantages: (a) analytical and numerical rotation tests have shown that the seven finite strain measures for granular materials are independent of rigid body rotation; (b) these formulations can also be used in the post-processing of experimental images to calculate strain for an assembly with a suitable particle tracking method (Ando et al., 2012; Druckrey and Alshibli, 2014); (c) higher order stress and strain formulations associated with finite strain micromorphic continua can be extended based upon these present formulations (Regueiro et al., 2014); and (d) the formulations derived here are easier to implement than the small strain measures, such as Bagi's strain (Bagi, 1996), especially in three dimensions (3D) (although Bagi's strain tensor is not valid for large deformation). The method to calculate stress within a granular assembly is based upon the well-known stress formulations of Christoffersen et al. (1981), Rothenburg and Selvadurai (1981) and Bagi (1996).

The two numerical examples have shown that the granular finite strain measures can be used to represent large deformations, and in particular the *rate-form* measures provide more realistic values. The results of a cavity expansion example have shown clearly the large strains associated with the three different phases of expansion simulation. A sub-domain has been used in the analysis of pile penetration, where local large deformation has been captured. With regard to constitutive modeling for these complicated numerical simulations involving particulate materials using DEM, we have shown how stress and strain curves can be generated in the finite strain regime, which will support constitutive model development in future work.

In conclusion, the *rate-form* calculation of the average deformation gradient over the tessellation, $\overline{\boldsymbol{F}}_{n+1}$ (which, in turn, can be used to calculate any finite strain measure), which is integrated from the average velocity gradient $\overline{\boldsymbol{l}}_{n+1}$, together they ($\overline{\boldsymbol{F}}_{n+1}$ and $\overline{\boldsymbol{l}}_{n+1}$) provide the general kinematics needed to formulate hierarchical multiscale constitutive models for granular media deforming/flowing at large deformations.

Acknowledgements

Funding for this research was provided by ONR MURI grant N00014–11-1–0691. This funding is gratefully acknowledged.

Appendix A. Tetrahedral volume and coordinate parameters

Recall that V^{tet} is the reference volume of the tetrahedron, such that,

$$V^{tet} = \frac{1}{6} det \begin{bmatrix} 1 & 1 & 1 & 1 \\ X_1^a & X_1^b & X_1^c & X_1^d \\ X_2^a & X_2^b & X_2^c & X_2^d \\ X_3^a & X_3^b & X_3^c & X_3^d \end{bmatrix} \tag{34}$$

and the global coordinate parameters used in Eq. (3) are,

$$\begin{aligned}
\omega_a &= X_2^b(X_3^d - X_3^c) - X_2^c(X_3^d - X_3^b) + X_2^d(X_3^c - X_3^b) \\
\theta_a &= -X_1^b(X_3^d - X_3^c) + X_1^c(X_3^d - X_3^b) - X_1^d(X_3^c - X_3^b) \\
\pi_a &= X_1^b(X_2^d - X_2^c) - X_1^c(X_2^d - X_2^b) + X_1^d(X_2^c - X_2^b) \\
\\
\omega_b &= -X_2^a(X_3^d - X_3^c) + X_2^c(X_3^d - X_3^a) - X_2^d(X_3^c - X_3^a) \\
\theta_b &= X_1^a(X_3^d - X_3^c) - X_1^c(X_3^d - X_3^a) + X_1^d(X_3^c - X_3^a) \\
\pi_b &= -X_1^a(X_2^d - X_2^c) + X_1^c(X_2^d - X_2^a) - X_1^d(X_2^c - X_2^a) \\
\\
\omega_c &= X_2^a(X_3^d - X_3^b) - X_2^b(X_3^d - X_3^a) + X_2^d(X_3^b - X_3^a) \\
\theta_c &= -X_1^a(X_3^d - X_3^b) + X_1^b(X_3^d - X_3^a) - X_1^d(X_3^b - X_3^a) \\
\pi_c &= X_1^a(X_2^d - X_2^b) - X_1^b(X_2^d - X_2^a) + X_1^d(X_2^b - X_2^a) \\
\omega_d &= -X_2^a(X_3^c - X_3^b) + X_2^b(X_3^c - X_3^a) - X_2^c(X_3^b - X_3^a) \\
\theta_d &= X_1^a(X_3^c - X_3^b) - X_1^b(X_3^c - X_3^a) + X_1^c(X_3^b - X_3^a) \\
\pi_d &= -X_1^a(X_2^c - X_2^b) + X_1^b(X_2^c - X_2^a) - X_1^c(X_2^b - X_2^a)
\end{aligned} \tag{35}$$

where $X_I^\alpha, I = 1,2,3, \alpha = a,b,c,d$ are the nodal coordinates of the tetrahedron in the reference configuration (Felippa, 2011), corresponding to the particle centroids in the reference state.

Appendix B. Analytical proof of invariance of granular finite strain formulations calculated from linear tetrahedron tessellation interpolation

For the linear tetrahedral tessellation interpolation, the granular Lagrangian strain, and granular Eulerian strain formulations are shown analytically to be free of a rigid body rotation. From Eq. (31), one can see that the granular displacement gradient tensor $\left(\overline{\frac{\partial \boldsymbol{u}}{\partial \boldsymbol{X}}}\right)$(take the Lagrangian strain formulation as an example) needs to be equal to $(\boldsymbol{Q}-\boldsymbol{1})$ to replicate a rigid body rotation exactly, and thus its strain be independent of this rotation. Then, (i) the individual displacement gradient tensor of each linear tetrahedron will be shown to be equal to $(\boldsymbol{Q}-\boldsymbol{1})$, and (ii) the granular displacement gradient tensor $\overline{\frac{\partial \boldsymbol{u}}{\partial \boldsymbol{X}}}$ for the assembly will be considered.

(i) Lagrangian displacement gradient tensor $\frac{\partial \boldsymbol{u}}{\partial \boldsymbol{X}}$ for individual linear tetrahedron From the kinematics of rigid body rotation in Eq. (30), one can obtain,

$$\boldsymbol{u}=\boldsymbol{x}-\boldsymbol{X}=\boldsymbol{Q}\boldsymbol{X}-\boldsymbol{X}=(\boldsymbol{Q}-\boldsymbol{1})\boldsymbol{X} \tag{36}$$

Substituting Eq. (36) into the formulation of displacement gradient tensor, Eq. (3), we have,

$$\frac{\partial \boldsymbol{u}}{\partial \boldsymbol{X}}=(\boldsymbol{Q}-\boldsymbol{1})\begin{bmatrix}\boldsymbol{X}^a & \boldsymbol{X}^b & \boldsymbol{X}^c & \boldsymbol{X}^d\end{bmatrix}\begin{bmatrix}\omega_a & \theta_a & \pi_a\\ \omega_b & \theta_b & \pi_b\\ \omega_c & \theta_c & \pi_c\\ \omega_d & \theta_d & \pi_d\end{bmatrix}\frac{1}{6V^{tet}} \tag{37}$$

To prove that $\frac{\partial \boldsymbol{u}}{\partial \boldsymbol{X}}$ is equal to $(\boldsymbol{Q}-\boldsymbol{1})$, we can show that,

$$\begin{bmatrix}\boldsymbol{X}^a & \boldsymbol{X}^b & \boldsymbol{X}^c & \boldsymbol{X}^d\end{bmatrix}\begin{bmatrix}\omega_a & \theta_a & \pi_a\\ \omega_b & \theta_b & \pi_b\\ \omega_c & \theta_c & \pi_c\\ \omega_d & \theta_d & \pi_d\end{bmatrix}\frac{1}{6V^{tet}}=\boldsymbol{1} \tag{38}$$

where coefficients $\omega_\alpha,\theta_\alpha,\pi_\alpha$, and V^{tet} are all based upon the reference configuration coordinates. With the help of the symbolic functions in Matlab, we can define the coordinates of four vertices of a *tet*as symbolic variables, and then substitute the four sets of coordinates into Eqs. (34) and (35) in Appendix A, and then into the left-hand-side of Eq. (38), where it is shown that Eq. (38) holds exactly. The Lagrangian displacement gradient tensor $\left(\frac{\partial \boldsymbol{u}}{\partial \boldsymbol{X}}\right)$ for every tetrahedron will be exactly the same $(\boldsymbol{Q}-\boldsymbol{1})$ if all the particles in the assembly follow the same rotation in Eq. (30). This is no surprise, as the linear tetrahedron is shown to be complete to first order (Hughes, 1987), meaning its shape functions can represent exactly rigid body motion (translation and rotation), as well as constant strain.

(ii) Granular Lagrangian displacement gradient tensor $\left(\overline{\frac{\partial \boldsymbol{u}}{\partial \boldsymbol{X}}}\right)$ over the sub-domain. We take the volume average of the displacement gradient tensor $\left(\frac{\partial \boldsymbol{u}}{\partial \boldsymbol{X}}\right)$ of all the tetrahedrons in the tessellation to obtain the granular Lagrangian displacement gradient tensor $\left(\overline{\frac{\partial \boldsymbol{u}}{\partial \boldsymbol{X}}}\right)$ over the sub-domain as,

$$\overline{\frac{\partial \boldsymbol{u}}{\partial \boldsymbol{X}}}=\frac{1}{\sum_{tet}V^{tet}}\sum_{tet}\left[\frac{\partial \boldsymbol{u}}{\partial \boldsymbol{X}}V^{tet}\right]=\frac{1}{\sum_{tet}V^{tet}}\frac{\partial \boldsymbol{u}}{\partial \boldsymbol{X}}\sum_{tet}V^{tet}=\frac{\partial \boldsymbol{u}}{\partial \boldsymbol{X}}=\boldsymbol{Q}-\boldsymbol{1} \tag{39}$$

The granular Eulerian displacement gradient tensor $\left(\overline{\frac{\partial \boldsymbol{u}}{\partial \boldsymbol{x}}}\right)$ can also be proved to be equal to $\left(\boldsymbol{1}-\boldsymbol{Q}^{-1}\right)$ following the same steps, which will guarantee that the granular Eulerian strain will be independent of rigid body rotation.

Appendix C. 2D triangle rotation example

C.1. Rotation in-the-plane

Suppose we rotate a triangle (but the relative vertex distances are unchanged, i.e., no deformation) in its plane by $\pi/2$ about vertex 1, as in Fig. 28, then the granular strain of this triangular tessellation can be calculated by Bagi's strain formulation as follows. If Bagi's strain tensor were an acceptable finite strain measure, it should generate zero strain values. As shown in the figure, the displacements of the three vertices are

$$\boldsymbol{u}^{(1)}=\begin{bmatrix}0\\0\end{bmatrix}\quad \boldsymbol{u}^{(2)}=\begin{bmatrix}1\\1\end{bmatrix}\quad \boldsymbol{u}^{(3)}=\begin{bmatrix}-2\\2\end{bmatrix} \tag{40}$$

At present, we assume the complementary area vector, $\boldsymbol{d}^{pq}$, is calculated based upon the current configuration. Then the outward area-vector of the vertices, $\boldsymbol{b}^{p}$, will be,

$$\boldsymbol{b}^{(1)}=\begin{bmatrix}2\\1\end{bmatrix}\quad \boldsymbol{b}^{(2)}=\begin{bmatrix}-2\\0\end{bmatrix}\quad \boldsymbol{b}^{(3)}=\begin{bmatrix}0\\-1\end{bmatrix} \tag{41}$$

For the three edges, the $\Delta\boldsymbol{u}^{pq}$ and $\boldsymbol{d}^{pq}$ will be,

1. edge 1–2, $\Delta\boldsymbol{u}^{12}=\begin{bmatrix}-1\\-1\end{bmatrix}$ and $\boldsymbol{d}^{12}=\frac{1}{6}\left(\boldsymbol{b}^{(2)}-\boldsymbol{b}^{(1)}\right)=\frac{1}{6}\begin{bmatrix}-4\\-1\end{bmatrix}$
2. edge 1–3, $\Delta\boldsymbol{u}^{13}=\begin{bmatrix}2\\-2\end{bmatrix}$ and $\boldsymbol{d}^{13}=\frac{1}{6}\left(\boldsymbol{b}^{(3)}-\boldsymbol{b}^{(1)}\right)=\frac{1}{6}\begin{bmatrix}-2\\-2\end{bmatrix}$
3. edge 2–3, $\Delta\boldsymbol{u}^{23}=\begin{bmatrix}3\\-1\end{bmatrix}$ and $\boldsymbol{d}^{23}=\frac{1}{6}\left(\boldsymbol{b}^{(3)}-\boldsymbol{b}^{(2)}\right)=\frac{1}{6}\begin{bmatrix}2\\-1\end{bmatrix}$

Following the formulation of Bagi in Eq. (1), the average displacement gradient is,

$$\overline{\nabla(\boldsymbol{u})}=\frac{1}{V}\sum_{p<q}\Delta u_i^{pq}d_j^{pq}=\begin{bmatrix}1 & -1\\ 1 & 1\end{bmatrix} \tag{42}$$

Then the granular strains based upon Bagi's formulation for this rotation example will be,

$$\frac{1}{2}\left(\overline{\nabla(\boldsymbol{u})}+\overline{\nabla(\boldsymbol{u})}^T-\overline{\nabla(\boldsymbol{u})}^T\overline{\nabla(\boldsymbol{u})}\right)=\begin{bmatrix}0 & 0\\ 0 & 0\end{bmatrix} \tag{43}$$

The finite strain extension of Bagi's strain provides **0** strain value, which is correct for this case of in-plane rotation of the triangle.

Similarly, if we calculate the complementary area vector, $\boldsymbol{d}^{pq}$, based upon the reference configuration, we have for the Bagi finite strain values,

$$\frac{1}{2}\left(\overline{\nabla(\boldsymbol{u})}+\overline{\nabla(\boldsymbol{u})}^T+\overline{\nabla(\boldsymbol{u})}^T\overline{\nabla(\boldsymbol{u})}\right)=\begin{bmatrix}0 & 0\\ 0 & 0\end{bmatrix} \tag{44}$$

C.2. Rotation out-of-the-plane

We now consider an out-of-the-plane rotation about the 1–3 edge, as shown in Fig. 29. If we calculate the complementary area vector, $\boldsymbol{d}^{pq}$, based upon the current configuration, we have for the Bagi strain values,

$$\begin{aligned}
\tfrac{1}{2}\left(\overline{\nabla(\boldsymbol{u})}+\overline{\nabla(\boldsymbol{u})}^{T}\right) &= \begin{bmatrix}0&0&0\\0&0&0.5\\0&0.5&1\end{bmatrix}\\
\tfrac{1}{2}\left(\overline{\nabla(\boldsymbol{u})}+\overline{\nabla(\boldsymbol{u})}^{T}-\overline{\nabla(\boldsymbol{u})}^{T}\overline{\nabla(\boldsymbol{u})}\right) &= \begin{bmatrix}0&0&0\\0&0&0.5\\0&0.5&0\end{bmatrix}\\
\tfrac{1}{2}\left(\overline{\nabla(\boldsymbol{u})}+\overline{\nabla(\boldsymbol{u})}^{T}+\overline{\nabla(\boldsymbol{u})}^{T}\overline{\nabla(\boldsymbol{u})}\right) &= \begin{bmatrix}0&0&0\\0&0&0.5\\0&0.5&2\end{bmatrix}
\end{aligned} \tag{45}$$

If we calculate the complementary area vector, $\boldsymbol{d}^{pq}$, based upon the reference configuration, we have for the Bagi strain values,

$$\begin{aligned}
\tfrac{1}{2}\left(\overline{\nabla(\boldsymbol{u})}+\overline{\nabla(\boldsymbol{u})}^{T}\right) &= \begin{bmatrix}0&0&0\\0&-1&-0.5\\0&-0.5&0\end{bmatrix}\\
\tfrac{1}{2}\left(\overline{\nabla(\boldsymbol{u})}+\overline{\nabla(\boldsymbol{u})}^{T}-\overline{\nabla(\boldsymbol{u})}^{T}\overline{\nabla(\boldsymbol{u})}\right) &= \begin{bmatrix}0&0&0\\0&-2&-0.5\\0&-0.5&0\end{bmatrix}\\
\tfrac{1}{2}\left(\overline{\nabla(\boldsymbol{u})}+\overline{\nabla(\boldsymbol{u})}^{T}+\overline{\nabla(\boldsymbol{u})}^{T}\overline{\nabla(\boldsymbol{u})}\right) &= \begin{bmatrix}0&0&0\\0&0&-0.5\\0&-0.5&0\end{bmatrix}
\end{aligned} \tag{46}$$

This out-of-the-plane rotation test proves that rigid body rotation represented by the Bagi strain formulation will lead to large erroneous values, as demonstrated in the numerical examples. The authors note that such analysis was not conducted on tetrahedra, which are the cell units used to calculate strain in the paper. However, this two-dimensional analysis provides insight into the limitations of extending Bagi's small strain tensor measure to finite strain, as illustrated by numerical examples in the paper.

References

Alshibli, K., Alramahi, B.A., 2006. Microscopic evaluation of strain distribution in granular materials during shear. J. Geotech. Geoenviron. Eng. 132 (1), 80–91.

Ando, E., Hall, S.A., Viggiani, G., Desrues, J., Bésuelle, P., 2012. Grain-scale experimental investigation of localised deformation in sand: a discrete particle tracking approach. Acta Geotech. 7 (1), 1–13.

Bagi, K., 1996. Stress and strain in granular assemblies. Mech. Mater. 22, 165–177.

Bagi, K., 2006. Analysis of microstructural strain tensors for granular assemblies. Int. J. Solids Struct. 43, 3166–3184.

Barber, C.B., Dobkin, D.P., Hudanpaa, H.T., 1996. The Quickhull algorithm for convex hulls. ACM Trans. Math. Software 22 (4), 469–483.

Bonelli, S., Millet, O., Nicot, F., Rahmoun, J., De Saxcé, G., 2012. On the definition of an average strain tensor for two-dimensional granular material assemblies. Int. J. Solids Struct. 49, 947–958.

Cambou, B., Chaze, M., Dedecker, F., 2000. Change of scale in granular materials. Eur. J. Mech. A/Solids 19, 999–1014.

Chang, C.S., Chang, Y., Kabir, M.G., 1992. Micromechanics modeling for stress–strain behavior of granular soils I: theory. J. Geotech. Eng. Div ASCE 118 (12), 1959–1974.

Christoffersen, J., Mehrabadi, M.M., Nemat-Nasser, S., 1981. A micromechanical description of granular material behavior. J. Appl. Mech. 48, 339–344.

Chupin, O., Rechenmacher, A.L., Abedi, S., 2012. Finite strain analysis of nonuniform deformation inside shear bands in sands. Int. J. Numer. Anal. Methods Geomech. 36, 1651–1666.

Dedecker, F., Chaze, M., Dubujet, Ph., Cambou, B., 2000. Specific features of strain in granular materials. Mech. Cohes.-Frict. Mater. 5, 173–193.

Druckrey, A.M., Alshibli, K.A., 2014. 3D behavior of sand particles using X-ray synchrotron micro-tomography. In: Abu-Farsakh, M. (Ed.), Geo-Congress 2014 Technical Papers: Geo-Characterization and Modeling for Sustainability. American Society of Civil Engineers, pp. 2814–2821.

Duran, O., Kruyt, N.P., Luding, S., 2010. Analysis of three-dimensional micro-mechanical strain tensor for granular materials: evaluation of accuracy. Int. J. Solids Struct. 47, 251–260.

Eringen, A.C., 1962. Nonlinear Theory of Continuous Media, first ed. McGraw-Hill.

Felippa, C.A., 2011. The linear tetrahedron. <http://www.colorado.edu/engineering/CAS/courses.d/AFEM.d/AFEM.Ch09.d/AFEM.Ch09.pdf>.

Fu, P., Dafalias, Y.F., 2012. Quantification of large and localized deformation in granular materials. Int. J. Solids Struct. 49, 1741–1752.

Holzapfel, G.A., 2000. Nonlinear Solid Mechanics: A Continuum Approach for Engineering. John Wiley & Sons.

Hughes, T.J.R., 1987. The Finite Element Method. Prentice-Hall, New Jersey.

Kruyt, N.P., 2003. Statics and kinematics of discrete Cosserat-type granular materials. Int. J. Solids Struct. 40, 511–534.

Kruyt, N.P., Rothenburg, L., 1996. Micromechanical definition of the strain tensor for granular materials. J. Appl. Mech. 118, 706–711.

Kuhn, M.R., 1999. Structured deformation in granular materials. Mech. Mater. 31, 407–429.

Liao, C.-L., Chang, T.-P., Young, D.-H., 1997. Stress–strain relationship for granular materials based on the hypothesis of best fit. Int. J. Solids Struct. 34 (31–32), 4087–4100.

O'Sullivan, C., Bray, J.D., Li, S., 2003. A new approach for calculating strain for particulate media. Int. J. Numer. Anal. Methods Geomech. 27, 859–877.

Regueiro, R.A., Yan, B., 2011. Concurrent multiscale computational modeling for dense dry granular materials interfacing deformable solid bodies. In: Wan, R., Alsaleh, M., Labuz, J. (Eds.), Bifurcations, Instabilities and Degradations in Geomaterials, Springer Series in Geomechanics and Geoengineering. Springer-Verlag, pp. 251–273.

Regueiro, R.A., Yan, B., 2013. Computational homogenization and partial overlap coupling between micropolar elastic continuum finite elements and elastic spherical discrete elements in one dimension. In: Li, S., Gao, X.-L. (Eds.), Handbook of Micromechanics and Nanomechanics, vol. 1. Pan Stanford Pub., pp. 1–45.

Regueiro, R.A., Pak, R., Sture, S., Vasilyev, O., McCartney, J., Yan, B., Duan, Z., Kasimov, N., Hansen, C., Svoboda, J., Mun, W.-J., Brown-Dymkoski, E., Li, S., Ren, B., Alshibli, K., Druckrey, A., Lu, H., Luo, H., Brannon, R., Bonifasi-Lista, C., Yarahmadi, A., Ghodrati, E., Colovos, J., 2013. ONR MURI project on soil blast modeling and simulation. In: Song, B., et al. (Ed.), Dynamic Behavior of Materials, Proceedings of the 2013 Annual Conference on Experimental and Applied Mechanics, vol. 1. pp. 341–353.

Regueiro, R.A., Zhang, B., Shahabi, F., 2014. Micromorphic continuum stress measures calculated from three-dimensional ellipsoidal discrete element simulations on granular media. In: Soga, K. (Ed.), International Symposium on Geomechanics from Micro to Macro: IS-Cambridge 2014. Cambridge, UK.

Rothenburg, L., Selvadurai, A.P.S., 1981. Micromechanical definition of the Cauchy stress tensor for particulate media. In: Selvadurai, A.P.S. (Ed.), Mechanics of Structured Media. Elsevier Scientific, pp. 469–486.

Satake, M., 2004. Tensorial form definitions of discrete-mechanical quantities for granular assemblies. Int. J. Solids Struct. 41, 5775–5791.

Tordesillas, A., Walsh, S.D.C., Muthuswamy, M., 2010. The effect of local kinematics on the local and global deformations of granular systems. Math. Mech. Solids 15 (1), 3–41.

Truesdell, C., Toupin, R.A., 1960. The classical field theories. Handbuch der Physik. Springer, Berlin.

Underwood, P., 1983. Dynamic relaxation. In: Belytschko, T., Hughes, T.J.R. (Eds.), Computational Methods for Transient Analysis. North-Holland, Amsterdam, pp. 245–265.

Yan, B., Regueiro, R.A., Sture, S., 2010. Three-dimensional ellipsoidal discrete element modeling of granular materials and its coupling with finite element facets. Eng. Comput. 27 (4), 519–550.